ORIGINAL PAPER



Low Static Shear Modulus Along Foliation and Its Influence on the Elastic and Strength Anisotropy of Poorman Schist Rocks, Homestake Mine, South Dakota

Katherine J. Condon¹ · Hiroki Sone¹ · Herbert F. Wang¹ · EGS CollabTeam

Received: 3 December 2019 / Accepted: 17 June 2020 / Published online: 9 August 2020 © Springer-Verlag GmbH Austria, part of Springer Nature 2020

Abstract

We investigate the influence of foliation orientation and fine-scale folding on the static and dynamic elastic properties and unconfined strength of the Poorman schist. Measurements from triaxial and uniaxial laboratory experiments reveal a significant amount of variability in the static and dynamic Young's modulus depending on the sample orientation relative to the foliation plane. Dynamic P-wave modulus and S-wave modulus are stiffer in the direction parallel to the foliation plane as expected for transversely isotropic mediums with average Thomsen parameters values 0.133 and 0.119 for epsilon and gamma, respectively. Static Young's modulus varies significantly between 21 and 117 GPa, and a peculiar trend is observed where some foliated sample groups show an anomalous decrease in the static Young's modulus when the symmetry axis $(x_3$ -axis) is oriented obliquely to the direction of loading. Utilizing stress and strain relationships for transversely isotropic medium, we derive the analytical expression for Young's modulus as a function of the elastic moduli E_1 , E_3 , ν_{31} , and G_{13} and sample orientation to fit the static Young's modulus measurements. Regression of the equation to the Young's modulus data reveals that the decrease in static Young's modulus at oblique symmetry axis orientations is directly influenced by a low shear modulus, G_{13} , which we attribute to shear sliding along foliation planes during static deformation that occurs as soon as the foliation is subject to shear stress. We argue that such difference between dynamic and static anisotropy is a characteristic of near-zero porosity anisotropic rocks. The uniaxial compressive strength also shows significant variability ranging from 21.9 to 194.6 MPa across the five sample locations and is the lowest when the symmetry axis is oriented 45° or 60° from the direction of loading, also a result of shear sliding along foliation planes during static deformation.

Keywords Anisotropy · Schist · Young's modulus · EGS Collab

Lis	et of Symbols	$\sigma_{ m Ax.~Diff}$	Axial differential stress (total stress-confin-
θ	Angle between symmetry axis and the		ing pressure)
	wave propagation direction or the loading	P_{C}	Confining pressure
	direction	arepsilon	Strain when discussed with stress or com-
ρ	Density		pliance and stiffness
X_3	Axis of rotational symmetry		Thomsen parameter describing the differ-
E	Young's modulus		ence in the P-wave velocities measured
ν	Poisson's ratio		parallel and perpendicular to the symmetry
G	Shear modulus		axis, normalized by the velocity at $\theta = 0^{\circ}$
M	P-wave modulus	C	Stiffness matrix
N	Constant used in equations for V_P , V_{SV} , V_{SH}	c_{ijkl}	Components of the stiffness tensor
		$S^{"}$	Compliance matrix
		S_{ijkl}	Components of the compliance tensor
_		$V_{\rm P}, V_{\rm SV}, V_{\rm SH}$	Compressional, vertical shear, and horizon-
\bowtie	Hiroki Sone		tal shear velocities
	hsone@wisc.edu	$\alpha, \beta_{\mathrm{Thom}}$	Thomsen parameters that describe $V_{\rm P}$
1	University of Wisconsin-Madison, Madison, WI 53706, USA		and V_{SH} , respectively, for perpendicular orientation



Thomsen parameter that describes the γ difference in $V_{\rm SH}$ measured parallel and perpendicular to the symmetry axis, normalized by the velocity at $\theta = 0^{\circ}$ δ Thomsen parameter used with α to describe the normal moveout of $V_{\rm P}$ Uniaxial compressive strength $\sigma_{\rm c}$ A. BConstants describing the variation in uniaxial compressive strength Orientation of minimum uniaxial compres- θ_{\min} sive strength for each planar sample group

1 Introduction

In this paper, we report laboratory measurements for the unconfined strength and the static and dynamic elastic properties of the Poorman formation schists collected from the Enhanced Geothermal Systems Collaboration (EGS Collab) hydraulic stimulation experiment testbed on the 4850-ft level of the Sanford Underground Research Facility (SURF). Rock deformation measurements are an integral component to understanding the rock behavior at the field site—a key objective of the EGS Collab project (Kneafsey et al. 2019). Previous studies on layered rocks such as shales and schists consider the elastic properties to behave as a transversely isotropic (TI) medium (Jones and Wang 1981; Amadei 1996; Sayers 2010; Sone and Zoback 2013). This intrinsic anisotropy is often developed by preferential orientation of platy or needle-like minerals and bedding planes developed through sedimentation. Quantifying the degree to which anisotropy influences the mechanical properties of the rock is needed for accurate interpretations of field surveys and developing realistic geomechanical models. In addition to influencing elastic properties, there have been long-standing studies that find a reduction in rock strength when foliation or bedding is oriented diagonally to the principal stress direction (Jaeger 1960; McLamore and Gray 1967; Ramamurthy et al. 1993). The influence of anisotropy on rock strength could significantly influence interpretation of borehole breakouts for in situ stress and planning of hydraulic stimulation tests.

The mechanical properties of anisotropic rocks are frequently studied because of their importance in rock engineering. Laboratory tests primarily focus on rock strength, dynamic elastic properties, and static elastic properties with limited studies covering a range of foliation or bedding orientations (Read et al. 1987; Nasseri et al. 2003). Few laboratory studies have focused on fully describing the static elastic response of the five independent elastic constants for TI rocks (Amadei 1996; Homand et al. 1993). We derive an analytical expression for Young's modulus of a TI medium oriented obliquely to the direction of loading to indirectly

obtain the static shear modulus. We discuss the influence of stress on the elastic property measurements, influence of foliation orientation on rock strength and failure planes, and the influence of heterogeneity on laboratory measurements.

2 Background: Elastic Properties of Transversely Isotropic Medium

Disregarding the anisotropic properties of schist may lead to inaccurate determination of elastic properties and estimates of rock mass deformation. Therefore, it has become more common in rock mechanics literature to consider finely layered and foliated rocks, such as shales (Sayers 2010; Sone and Zoback 2013), phyllites, schists, and gneiss, as a TI medium with an axis of rotational symmetry perpendicular to the planar fabric. Here, we review the governing stress–strain relations for a TI medium and the Thomsen parameters used to describe the degree of anisotropy of a TI medium.

2.1 Elastic Constants

In contrast to an isotropic medium which has two independent elastic constants, TI mediums require five independent elastic constants to fully describe its mechanical properties. Hooke's law for an anisotropic, linear, elastic solid relates the linear proportionality between stress and strain by Eq. (1) where the elements of the elastic stiffness tensor are denoted as c_{ijkl} .

$$\sigma_{ij} = c_{ijkl} \varepsilon_{kl} . \tag{1}$$

Due to symmetry of stress and strain tensors and the presence of a unique strain energy potential, $c_{ijkl} = c_{jilk} = c_{jilk} = c_{jilk} = c_{jilk} = c_{jilk}$ and $c_{ijkl} = c_{klij}$, which reduce the total number of independent elastic constants from 81 to 21 components (Mavko et al. 2009). Considering the X_3 -axis to be the axis of rotational symmetry, the nonzero elastic stiffness tensor for a TI medium can be simplified and written in matrix form using the two-index Voigt notation (Nye 1985). The independent stiffness constants required to fully describe the mechanical properties of a material in Eq. (1) are c_{11} , c_{33} , c_{12} , c_{13} , and c_{44} .

$$C = \begin{bmatrix} c_{11} & c_{12} & c_{13} & 0 & 0 & 0 \\ c_{12} & c_{11} & c_{13} & 0 & 0 & 0 \\ c_{13} & c_{13} & c_{33} & 0 & 0 & 0 \\ 0 & 0 & 0 & c_{44} & 0 & 0 \\ 0 & 0 & 0 & 0 & 0 & c_{66} \end{bmatrix}$$
 (2)



with
$$c_{66} = \frac{1}{2}(c_{11} - c_{12})$$
.

with $c_{66} = \frac{1}{2}(c_{11} - c_{12})$. The stiffness matrix (Eq. 2) is the inverse of the compliance matrix (S) as shown in the following equation:

$$C = S^{-1} . (3)$$

Conveniently, the compliance matrix can be written in terms of the Young's modulus (E), Poisson's ratio (ν), and shear modulus (G) for a TI medium as

$$S = \begin{bmatrix} \frac{1}{E_{1}} & -\frac{v_{12}}{E_{1}} & -\frac{v_{31}}{E_{3}} & 0 & 0 & 0\\ -\frac{v_{12}}{E_{1}} & \frac{1}{E_{1}} & -\frac{v_{31}}{E_{3}} & 0 & 0 & 0\\ -\frac{v_{13}}{E_{1}} & -\frac{v_{13}}{E_{1}} & \frac{1}{E_{3}} & 0 & 0 & 0\\ -\frac{v_{13}}{E_{1}} & -\frac{v_{13}}{E_{1}} & \frac{1}{E_{3}} & 0 & 0 & 0\\ 0 & 0 & 0 & \frac{1}{G_{13}} & 0 & 0\\ 0 & 0 & 0 & 0 & \frac{1}{G_{13}} & 0\\ 0 & 0 & 0 & 0 & 0 & \frac{1}{G_{12}} \end{bmatrix}. \tag{4}$$

The single subscript of the Young's modulus corresponds to the strain in axis X_i , Poisson's ratio ν_{ii} relates the strain in symmetry direction j to the applied strain in symmetry direction i, and shear modulus G_{ii} corresponds to the shear strain in plane $X_i X_i$ (Sayers 2010). Symmetry of the compliance matrix $S_{ij} = S_{ji}$ requires that $\nu_{21} = \nu_{12}$ and $E_3\nu_{13}$ $E_1\nu_{31}$. Determination of the elastic moduli E_1 , E_3 , ν_{31} and ν_{21} can be estimated through laboratory tests on vertically and horizontally layered rock where the symmetry axis, X_3 , is oriented parallel or perpendicular to the direction of differential stress loading.

2.2 Dynamic Stiffness Constants and Velocities

For a transversely isotropic medium, propagation modes of the three velocities $(V_P, V_{SV}, \text{ and } V_{SH})$ are described as quasilongitudinal, quasi-shear, and pure shear, respectively, with mutually orthogonal polarizations (Mavko et al. 2009). The angle between the direction of wave propagation and the symmetry axis (X_3) of the material is defined by the angle θ .

Figure 1 shows a schematic of a transversely isotropic material with the propagation and polarization directions for the shear velocities V_{SV} and V_{SH} .

The phase velocities in any plane containing the X_3 symmetry axis are related to the angle θ , the stiffness constants, and the density (ρ) of the medium by the following equations:

$$V_P = \left(c_{11}\sin^2\theta + c_{33}\cos^2\theta + c_{44} + \sqrt{N}\right)^{\frac{1}{2}} (2\rho)^{-\frac{1}{2}},\tag{5}$$

$$V_{SV} = \left(c_{11}\sin^2\theta + c_{33}\cos^2\theta + c_{44} - \sqrt{N}\right)^{\frac{1}{2}} (2\rho)^{-\frac{1}{2}}, \quad (6)$$

$$V_{SH} = \left(\frac{c_{66}\sin^2\theta + c_{44}\cos^2\theta}{\rho}\right)^{\frac{1}{2}},\tag{7}$$

where

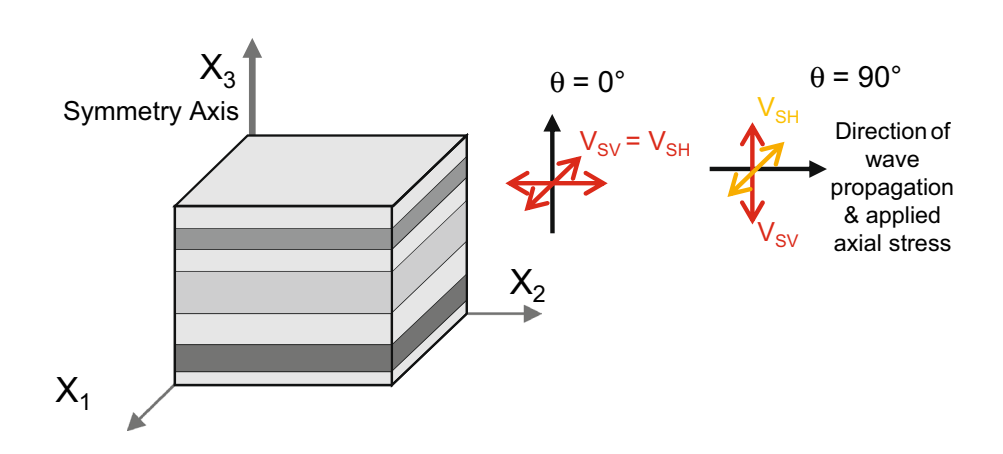
$$N = \left[\left(c_{11} - c_{44} \right) \sin^2(\theta) - \left(c_{33} - c_{44} \right) \cos^2 \theta \right]^2 + \left(c_{13} + c_{44} \right)^2 \sin^2 2\theta$$
(8)

(Thomsen 1986).

By measuring the velocity at multiple orientations of θ and assuming a constant material density, all five stiffness constants are resolved.

The degree of anisotropy of a TI medium is conveniently described in terms of the Thomsen parameters (α , β_{Thom} , ε , γ , and δ). Thomsen parameters α and $\beta_{\rm Thom}$ denote $V_{\rm P}$ and $V_{\rm SH}$, respectively, for $\theta = 0^{\circ}$. For a material with weak anisotropy, the parameter ε describes the difference in the P-wave velocities measured parallel and perpendicular to the symmetry axis, normalized by the velocity in the $\theta = 0^{\circ}$ direction, and is often described as the "P-wave anisotropy" parameter. The parameter γ describes the difference in V_{SH} measured parallel and perpendicular to the symmetry axis, normalized by the velocity in the $\theta = 0^{\circ}$ direction, and is often referred to as the "S-wave anisotropy" parameter. Both ε and γ typically range between 0 and 0.5 for weakly anisotropic rocks. The normal moveout of $V_{\rm p}$ is described with the parameters δ and α (Mavko et al. 2009). Although, in

Fig. 1 Schematic of a transversely isotropic (TI) medium showing the X_3 -axis of symmetry. Open arrows indicate the polarization direction of the shear velocities V_{SV} and V_{SH} with respect to the direction of wave propagation (closed arrow)





theory, δ can be constrained from a velocity measurement at one oblique orientation, it is best to measure the P-wave velocities at multiple orientations so that Eq. (5) can be fit to the entire dataset. From the stiffness constants and material density, the Thomsen parameters can be determined from the following equations:

$$\alpha = \sqrt{\frac{c_{33}}{\rho}} \,, \tag{9}$$

$$\beta_{\text{Thom}} = \sqrt{\frac{c_{44}}{\rho}},\tag{10}$$

$$\varepsilon = \frac{c_{11} - c_{33}}{2c_{33}} \,, \tag{11}$$

$$\gamma = \frac{(c_{66} - c_{44})}{2c_{44}} \,, \tag{12}$$

$$\delta = \frac{(c_{13} + c_{44})^2 - (c_{33} - c_{44})^2}{2c_{33}(c_{33} - c_{44})}$$
 (13)

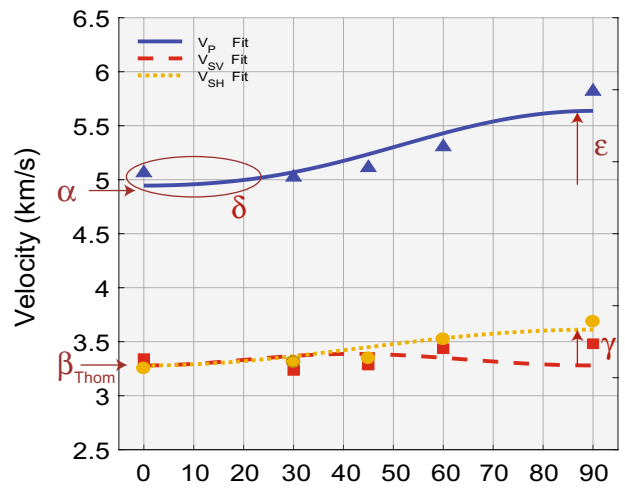
(Thomsen 1986).

Measurements of ultrasonic velocities ($V_{\rm P}$, $V_{\rm SV}$, and $V_{\rm SH}$) in directions θ =0°, 90°, and at least one angle between 0° and 90° provide data to which Eqs. (5) through (8) can be fit using least-square regression to determine stiffness constants. Given the best fit stiffness constants, the Thomsen parameters are determined from Eqs. (9) through (13) to conveniently describe the anisotropy of the material. Figure 2 shows an example of the velocity curve fit to ultrasonic velocity measurements obtained at different angles of θ as a visual representation of the Thomsen parameters.

2.3 Analytical Expression for Young's Modulus of Rotated TI Mediums

As seen in the previous sections, one can directly relate components of the compliance matrix to Young's modulus and Poisson's ratio through Eq. (4) when the direction of strain or stress is parallel or perpendicular to planar features in the rock. However, the influence of an oblique loading orientation with the symmetry axis on static Young's modulus is not examined frequently in the literature. The influence of layer orientation is a critical component to understanding the mechanical properties of dipping or folded structures. Here, we utilize stress and strain matrix rotation to solve for the resulting strain from a uniaxial stress condition ($\sigma_{33} \neq 0$). A complete derivation of the equations is presented in Appendix A.

The angle θ describes the orientation of the symmetry axis with respect to the direction of axial stress as shown in Fig. 1. Strain along the loading direction axis is needed to estimate the Young's modulus as a function of the rotation angle θ and the elastic moduli E_1, E_3, ν_{31} , and G_{13} :



Angle between X_3 and Wave Propagation, θ°

Fig. 2 Curve fit to velocity measurements at different orientations of θ . Using the best fit velocity curves and Eqs. (5) through (8), the best fit stiffness constants were obtained. Using the best fit stiffness constants, the Thomsen parameters $(\alpha, \beta_{\text{Thom}}, \varepsilon, \gamma, \delta)$ were obtained from Eqs. (9) through (13). Thomsen parameters conveniently describe P-wave anisotropy (ε) , S-wave anisotropy (γ) normal moveout of V_P (δ and α) and V_P and V_{SH} when $\theta = 0^\circ$ (α , β_{Thom} , respectively)

$$\varepsilon_{33} = \left(\frac{\sin^4 \theta}{E_1} - \frac{2\nu_{31}\sin^2 \theta \cos^2 \theta}{E_3} + \frac{\cos^4 \theta}{E_3} + \frac{\sin^2 \theta \cos^2 \theta}{G_{13}}\right)\sigma_{33}, \quad (14)$$

where

$$s_{11} = \frac{1}{E_1}, s_{13} = \frac{-v_{31}}{E_3}, s_{33} = \frac{1}{E_3}$$
 and $s_{44} = \frac{1}{G_{13}}$. (15)

Dividing the stress by strain in Eq. (14) leaves the expression for Young's modulus, which is in agreement with the equation for the evaluation of the shear modulus presented in Homand et al (1993). Note that there is a change in the Young's modulus from E_3 to E_1 in the denominator of the $\sin^4\theta$ term above, which corrects an error in a similar equation provided in Amadei (1996), also Eq. 14 in Amadei (1996). The presence of G_{13} in the analytical expression suggests that the static shear modulus in the 1–3 plane can be determined from a uniaxial stress compression measurement where the symmetry axis is oblique to the loading direction.

3 Laboratory Procedure

3.1 Sample Selection

3.1.1 Sample Group Locations and Preparation

The rocks in this study are situated in the Poorman formation which is a low-permeability, gray-to-black metasedimentary



rock. The mineralogy of the EGS Collab testbed is dominated by sericite—carbonate—quartz, biotite—quartz—carbonate, and graphitic quartz—sericite phyllite to schist (Caddey et al. 1991). There are significant heterogeneities throughout the formation including veins of quartz, carbonates, pyrite, and pyrrhotite, and foliation that varies from planar bands to tight folds at the centimeter to meter scale. The stress state at the 4850-foot-depth level of SURF is estimated at 42 MPa of vertical stress and 21 MPa of minimum horizontal stress from stress measurements in the kISMET project (Oldenburg et al. 2017; Wang et al. 2017), which was in close proximity to the EGS Collab testbed.

Five sections of HQ-sized host cores were selected from four boreholes lettered I, P, OB, and PDB. The borehole diagram showing the locations of the samples with respect to one another is provided in Appendix B (Fig. 17). Core logs and photographs were used to identify sections of competent host core that were at least 2 to 5 feet in length with consistent textural features. This allowed for groups of three-five samples to be prepared from the same few feet of host core to minimize variability between samples in a group. Using a tilting table to control the orientation of the cores, multiple cylindrical samples were sub-cored at different orientations from the same section of host core and trimmed to approximately 2-in. length and 1-in. diameter. To represent the various foliation textures observed in the field, three sample groups with planar foliation features and two sample groups with tightly folded foliation features were prepared.

Three sample groups with planar foliation were prepared from boreholes OB, P, and I. Each of the groups contained five samples which were sub-cored with axes at angles θ =0°, 30°, 45°, 60°, and 90°. The schematic diagram in Fig. 3a shows the definition of the θ angle and the appearance of the foliation. Planar sample names are assigned based on the borehole (P, I, or OB) and the θ orientation of the sample (0, 30, 45, 60, 90). Samples with θ =0° are occasionally referred to as "perpendicular" samples whereas samples with θ =90° are occasionally referred to as "parallel" samples.

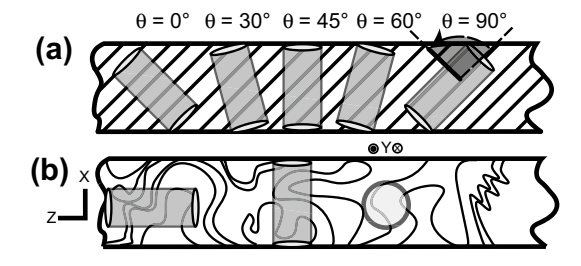


Fig. 3 Schematic diagram showing the orientation of the sub-cored samples relative to the host core. **a** Orientation of planar samples is defined by the θ angle. **b** Orientation of tightly folded cores are defined by orthogonal X-, Y-, and Z-axes

Sub-core locations were selected to maintain fabric consistency across samples within a group and avoid filled or open fractures and veins, except for OB30 which had a thin, white vein approximately 1 mm thick oriented 45° from the core axis. Photographs of the samples arranged by the sample group are shown in Fig. 4. General observations of each sample group's appearance suggest there may be minor mineralogical and textural differences between the three groups. Sample group P is light gray Poorman formation with less distinctive foliation bands compared to the other two groups. Group I is light to dark gray Poorman formation with distinctive foliation bands. The planar OB group has distinct foliation bands and is light gray to bronze-brown in color (OB60 in particular) suggesting there could be a slight mineralogical difference in the OB group compared to I and P.

Two groups of tightly folded core were prepared from boreholes PDB and OB. These cores were tightly folded at the centimeter scale so no dominant foliation orientation was observed. To avoid any orientation bias, samples were sub-cored for each group in orthogonal directions X, Y, or Z. Figure 3b shows the orientation of the sub-cored samples with respect to the host core. The Z-axis is parallel and X and Y are perpendicular to the host core axis. Folded sample names are assigned based on the borehole letters (PDB, OB) and axis orientation (X, Y, Z). Thus, planar and folded samples from the OB group are distinguished based on orientation described as numbers for the planar group or letters for the folded group.

3.1.2 Rock Characteristics

X-ray diffraction analysis provided quantitative measurements of mineralogy. The mineral distribution of the samples is between 18 and 57% mica, 14 and 43% quartz, 9 and 33% carbonates, 3 and 10% feldspar, 0 and 9% graphite, and trace amounts of sulfates, pyrite, and pyrrhotite. The distribution of mica minerals is between 7 and 33% muscovite, 1 and 19% chlorite, 2 and 11% illite, and 1 and 7% biotite. Representative photomicrographs from the three planar groups and one from folded group PDB are shown in Fig. 5. The white dashed line in the bottom-left corner of the three planar foliation photos designates the parallel orientation of the foliation planes. Variation in the continuity of planar foliation planes is observed between sample group P and groups I and OB.

The density of each sample was measured using a caliper and a digital mass balance after drying the samples in a vacuum oven for over 24 h. Density was averaged within each of the five sample groups and the total average (2.764 g/cc) and standard deviation (0.023 g/cc) for all groups are summarized in Table 1. Sample OB60 has a density (2.847 g/cc) more than one standard deviation above the average suggesting the sample may have a different mineral composition than the other samples. Due to the significantly



Fig. 4 Photographs of the samples prepared from five different borehole locations. The top three rows show the samples in the planar groups whereas the fourth row shows the two folded sample groups. Sample names are assigned based on borehole location (P, I, OB, or PDB) and orientation (e.g., 0, 45, *X*, *Z*)



different density, OB60 is considered an outlier from the sample group.

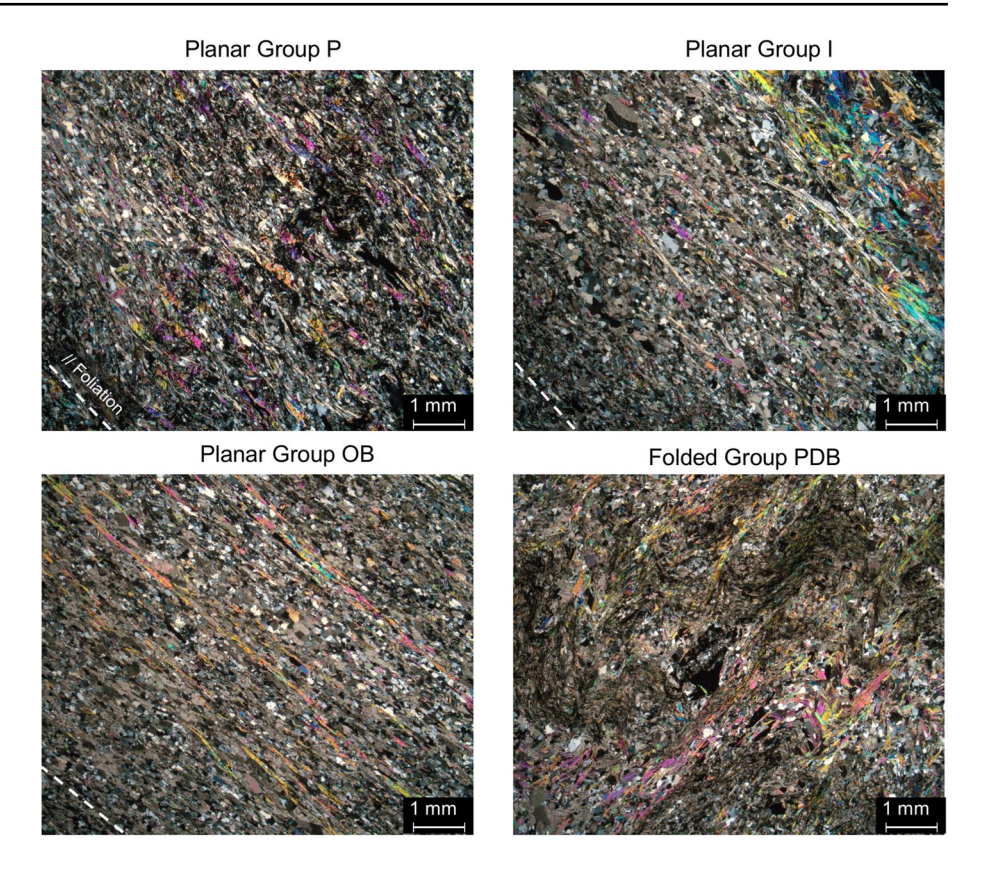
3.2 Laboratory Triaxial and Uniaxial Compression Tests

A programmable servo-controlled triaxial apparatus controlled confining pressure and axial load to deform the rocks under triaxial and uniaxial stress conditions. Figure 6 plots the stress path for $\sigma_{\rm Ax.\,Diff.}$ and $P_{\rm C}$ over time. During the first stage of the test, hydrostatic pressure was applied by increasing the confining pressure ($P_{\rm C}$) to 21 MPa to measure velocity anisotropy when all samples were under the same stress conditions. Then triaxial stress was applied by increasing the axial differential stress ($\sigma_{\rm Ax.\,Diff.} = \sigma_{\rm Ax.\,Total} - P_{\rm C}$) to 21 MPa.

The 42 MPa total axial stress ($\sigma_{\rm Ax.\ Total}$) and $P_{\rm C}$ = 21 MPa triaxial stress state is representative of the vertical stress and the in situ minimum horizontal stress, respectively, at the 4850-ft depth level of SURF as previously mentioned. The application of hydrostatic pressure before axial loading assists in the closure of microcracks from core damage sustained during drilling and removing the core from the in situ stress. Once the triaxial loading phase was complete, $\sigma_{\rm Ax.\ Diff.}$ was lowered to 1 MPa during the triaxial unloading stage followed by a release of the confining pressure. Finally, axial stress was applied at a constant strain rate of $10^{-5}~{\rm s}^{-1}$ until failure to measure the rock strength under unconfined conditions. The numbers and letters in Fig. 6 refer to the stresses at which elastic properties were measured and are further discussed in Sect. 4.3.



Fig. 5 Representative photomicrographs taken from each of the three planar sample groups and one folded sample from PDB. The white dashed line in the bottom left corner for the three planar foliation sample groups shows the parallel orientation of the foliation planes. Scale bars in the bottom right corner indicate 1 mm distance



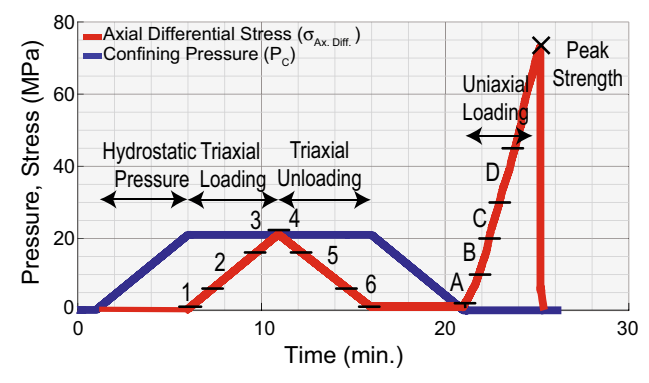


Fig. 6 Stress paths for confining pressure and axial differential stress over the duration of the test

Table 1 Summary table of the average density and standard deviation for each sample group and across all samples

Borehole	Group borehole depth (ft)	Avg. density (g/cc)	Standard deviation within group (g/cc)
E1-P	175–177	2.757	0.007
E1-I	150-155	2.764	0.012
E1-OB	85.5-89.5	2.778	0.042
E1-PDB	51–52	2.770	_
E1-OB	195–196	2.748	0.010
All samples		2.764	0.023

Rock deformation was measured using two pairs of 10-mm axial and radial strain gages applied directly on the sample. A polyolefin heat-shrink jacket was used to prevent confining oil from leaking into the rock. Ultrasonic velocity was sampled automatically at 1-min intervals throughout the test. Piezoelectric crystals attached to the loading platens were used to pulse and detect compressional and shear wave arrivals. Crystal frequency was 200 kHz except for sample group P which used a 1 MHz crystal due to equipment availability. A 1 MPa axial differential stress was maintained at all time to ensure coupling between the rock and the ultrasonic platen.

4 Results

4.1 Anisotropic Dynamic Elastic Properties

 $V_{\rm P}, V_{\rm SV}$, and $V_{\rm SH}$ for the planar sample groups and $V_{\rm P}, V_{\rm SI}$, and $V_{\rm S2}$ for the folded samples were measured under peak hydrostatic stress of 21 MPa. A hydrostatic or isotropic stress state is most appropriate to capture the intrinsic anisotropy of the rock fabric and to avoid any anisotropy that could be induced by a differential stress, as discussed later in detail. Figure 7 shows the velocity data points with the predicted velocity curves from the best fit dynamic stiffness



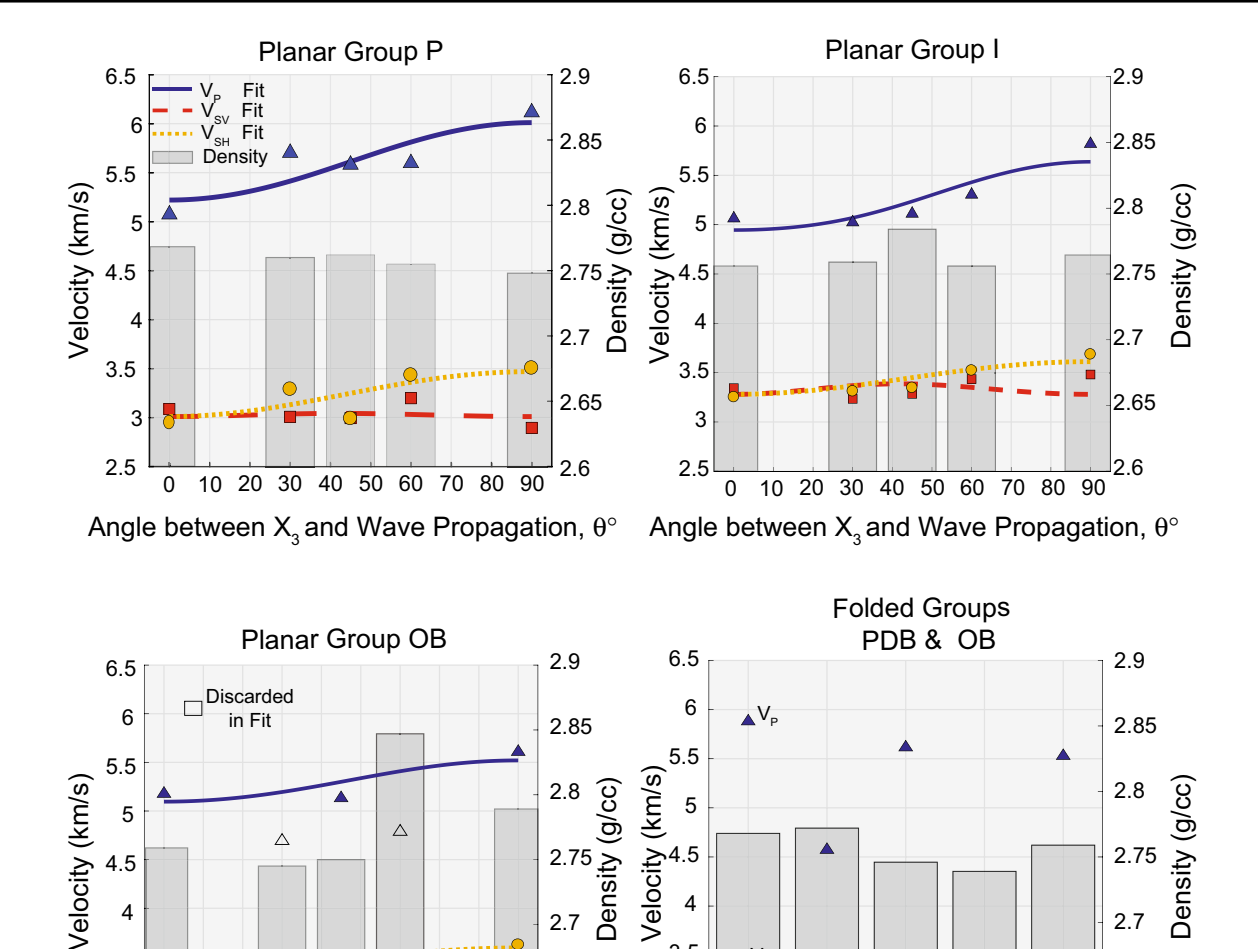


Fig. 7 Velocity for all sample groups taken under peak hydrostatic stress conditions ($P_C = \sigma_1 = \sigma_2 = \sigma_3 = 21$ MPa). The three planar sample groups show curves for velocity as a function of orientation resulting from a least-squares fit of Eqs. (5) through (8) to the velocity data

2.65

2.6

0 0

20 30 40 50 60 70 80 90

Angle between X_3 and Wave Propagation, θ°

3.5

3

2.5

PDB Y PDB Z

OB X

constants. Gray bars are aligned with each velocity measurement to show the density of each sample. Samples OB30 and OB60 were removed from the velocity curve fit due to having a significantly different density or presence of a textural feature as noted in Sect. 3.1. The best-fit dynamic stiffness constants determined from the velocity fit are shown in Table 2 along with the Thomsen parameters and elastic moduli.

O

3.5

3

Figure 7 clearly shows velocity anisotropy with foliation plane orientation for the three planar sample groups. Anisotropy parameters, ε and γ in Table 2, are within the expected range for anisotropic rocks indicating all three planar sample groups show P- and S-wave anisotropy. Higher values of ε and γ indicate velocity anisotropy is higher for sample group P than sample groups I and OB

under hydrostatic stress. Because the Thomsen parameters and elastic moduli are directly calculated from the stiffness constants, sample group P shows the highest amount of anisotropy in the dynamic Young's modulus compared to I and OB (Table 2).

OB Y

2.65

2.6

OB Z

Velocity measurements for four of the five folded samples were successfully obtained. The folded samples have a minimum $V_{\rm P}$ of 4.57 km/s and a maximum $V_{\rm P}$ of 5.88 km/s. This 25% difference in $V_{\rm P}$ is significant and suggests there are differences in the dynamic elastic properties of the folded rocks at the laboratory scale. While as a whole the four folded group samples show significant differences in velocity, samples OB X and OB Z from the same group show less variability in $V_{\rm P}$ (1.6%) compared to the two PDB samples. Significant differences in dynamic elastic properties



Table 2 Dynamic elastic properties determined from the velocity fit as a function of orientation using Eqs. (5) through (8). The average density of each sample group excluding outliers was used for the density parameter in the fit equations

Planar sample group		P	I	OB
Avg. density (g/cc)		2.757	2.764	2.766
c_{11} (GPa)		99.61	87.84	84.29
c_{33} (GPa)		75.14	67.60	71.84
c_{12} (GPa)		33.23	15.74	12.93
c_{13} (GPa)		35.10	13.19	16.28
c_{44} (GPa)	$=G_{23}=G_{13}$	24.99	29.73	30.32
c_{66} (GPa)	$=G_{12}=E_{11}/2(1+\nu_{12})$	33.19	36.05	35.68
α (km/s)		5.220	4.945	5.096
β (km/s)		3.010	3.280	3.311
ϵ		0.163	0.150	0.087
γ		0.164	0.106	0.088
δ		0.145	0.080	0.075
E_1 (GPa)		79.81	83.23	79.54
E_3 (GPa)		56.59	64.24	66.38
ν_{31}	$=\nu_{32}$	0.26	0.13	0.17
ν_{12}	$=\nu_{21}$	0.20	0.15	0.11
ν_{13}	$= \nu_{23} = E_1 \nu_{31} / E_3$	0.37	0.16	0.20

are associated with sample variability at the laboratory scale even when sampled from the same section of host core.

The sensitivity of the velocity measurements to heterogeneities is reflected in the dynamic elastic moduli provided in Table 3. To determine the dynamic elastic moduli, we assume an isotropic material behavior for the folded samples because the folded foliation follows no dominant orientation. The velocity and elastic moduli $(M = V_{\rm P}^2 \rho; G = V_{\rm S}^2 \rho)$ for sample PDB Z consistently exceed one standard deviation from the average value of all sample groups. This suggests that sample PDB Z is an outlier in the folded sample group and may be a result of textural heterogeneities.

4.2 Stress Dependence of Dynamic Elastic Properties on Planar Samples

The velocities of the planar samples were measured during triaxial loading and unloading to investigate the influence of stress on dynamic elastic properties. Figure 8 shows the normalized $V_{\rm P}$, $V_{\rm SV}$, and $V_{\rm SH}$ over time and marks the time of peak axial differential stress following triaxial loading with a dashed line. The loading history (Fig. 6) was the same for all samples, thus the stress was the same for all samples at the time–velocity measured.

Overall, all samples show an increase in velocity when axial differential stress is applied followed by a decrease in velocity when axial differential stress was unloaded as a result of closing and opening of microcracks in the sample. When comparing velocity changes within a sample group, we observe additional trends in the velocity response that depend on foliation orientation. Samples with a foliation orientation perpendicular (θ =0°) to the loading direction show a larger increase in normalized velocity with stress compared to samples with a parallel (θ =90°) orientation. This observation is attributed to more elongated microcracks aligned with the foliation of the sample, thus more crack-closure and sample stiffening occurs in the perpendicular samples.

While the above comparison between the parallel and perpendicular orientations is consistent across all sample groups, the normalized $V_{\rm SV}$ behavior of intermediate orientations is different for sample group P than for sample groups I and OB. The intermediate orientations for sample groups I and OB show enhanced stiffening compared to parallel and perpendicular orientations. At peak axial differential stress, the intermediate orientations generally have a higher normalized $V_{\rm SV}$ compared to the parallel and perpendicular orientations in sample groups I and OB (Fig. 9). In contrast, the intermediate orientations generally have a lower normalized $V_{\rm SV}$ compared to the parallel and perpendicular orientations in sample group P.

The I and OB intermediate orientations generally show enhanced hysteresis compared to the parallel and perpendicular orientations across nearly all normalized velocities. The enhanced hysteresis suggests there is additional irrecoverable strain occurring for the intermediate orientations in the I and OB sample groups which is not observed in the parallel and perpendicular samples. Sample group P does not exhibit this behavior as hysteresis did not show any dependence on orientation. This will be discussed in depth in Sect. 5.1.

Table 3 Compressional and shear velocity measurements of the folded sample with dynamic elastic moduli assuming isotropic material properties

Folded sample	Density (g/cc)	V _P (km/s)	V _{S1} (km/s)	V _{S2} (km/s)	Avg. $V_{\rm S}$ (km/s)	M (GPa)	G (GPa)
PDB Y	2.768	5.88	2.84	3.32	3.08	95.7	26.2
PDB Z	2.772	4.57	2.78	2.75	2.77	57.9	21.2
OB X	2.746	5.62	3.00	2.88	2.94	86.6	23.7
OB Y	2.739	_	_	_	_	_	_
OB Z	2.759	5.53	3.09	3.14	3.12	84.3	26.8
Avg	2.76	5.40	2.93	3.02	2.98	81.1	24.5
Std. dev.	0.01	0.57	0.14	0.26	0.16	16.2	2.6



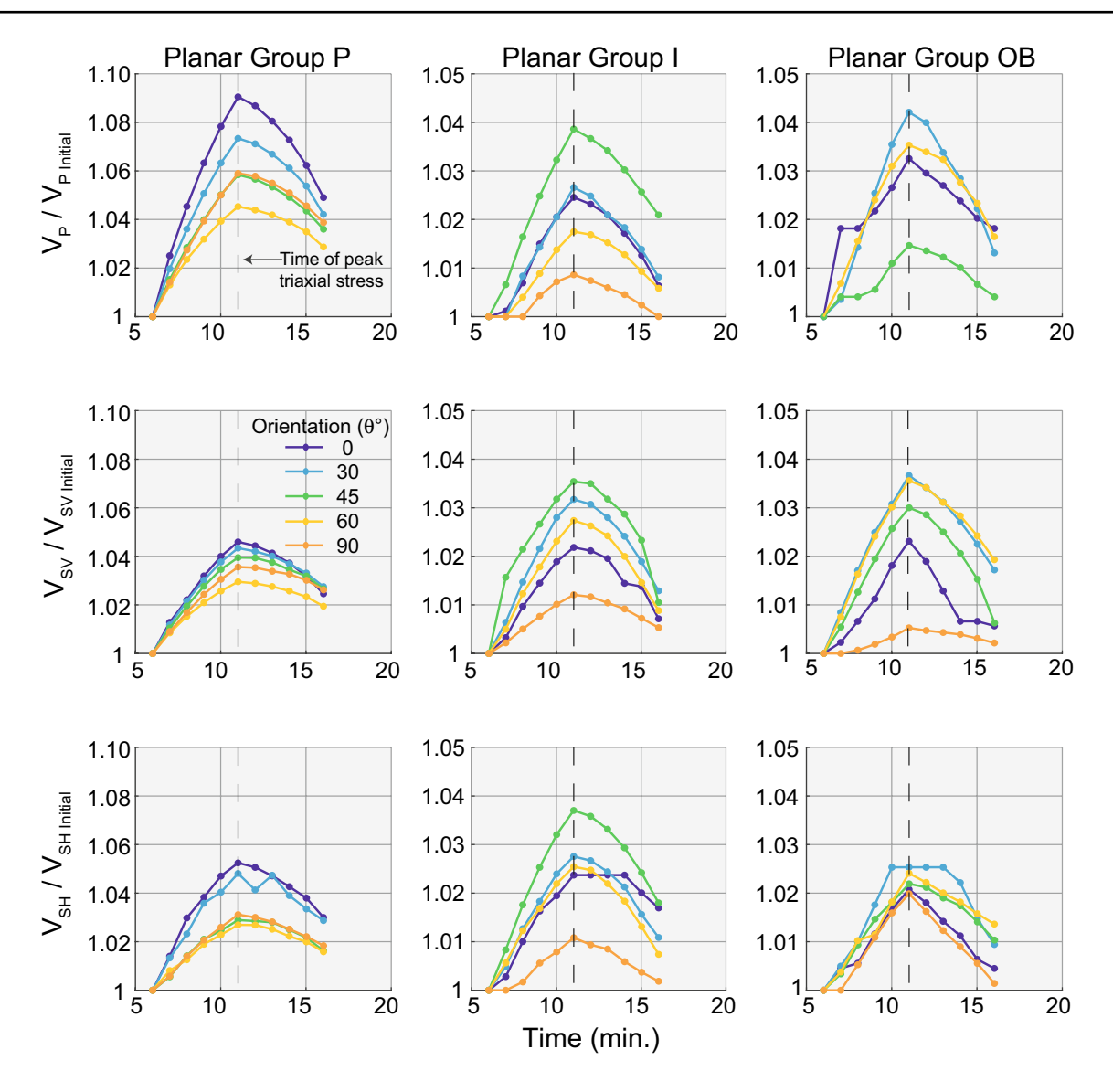


Fig. 8 V_P , V_{SV} , and V_{SH} normalized with the velocity at the start of the triaxial loading stage. The normalized velocities are plotted against time to show the velocity evolution during triaxial loading

and unloading stages. The dashed line marks the time when triaxial loading completed and unloading begins

4.3 Static Young's Modulus and Poisson's Ratio

Young's modulus (E) and Poisson's ratio (ν) were measured during three main stages of the test stress path: triaxial loading, triaxial unloading, and uniaxial loading. Each stress path stage was further subdivided into several ranges of $\sigma_{\rm Ax.\,Diff.}$ to characterize elastic properties at different stress levels. Table 4 summarizes the stress path, confining pressure, range of $\sigma_{\rm Ax.\,Diff.}$, and a number or letter used to distinguish the stages. Young's modulus was determined by linear regression of the strain data between initial and final $\sigma_{\rm Ax.\,Diff.}$ and the Poisson's ratio was calculated at the final $\sigma_{\rm Ax.\,Diff.}$ reported in the table. Figure 10 shows the static Young's

modulus for each sample measured during the stress path stages in Table 4.

Young's modulus measured near in situ stress conditions (stress stage 3) ranges approximately between 39 and 100 GPa. Previous measurements on parallel and perpendicular Poorman formation samples located nearby showed Young's modulus values between 45.1 and 87.2 GPa (Vigilante 2017) suggesting measurements in this study are consistent with previous measurements. A complete table of static Young's modulus measurements, averages, and standard deviations for each stress stage is provided in Appendix C.

Across the three planar sample groups, the parallel orientation ($\theta = 90^{\circ}$) generally has a higher Young's modulus



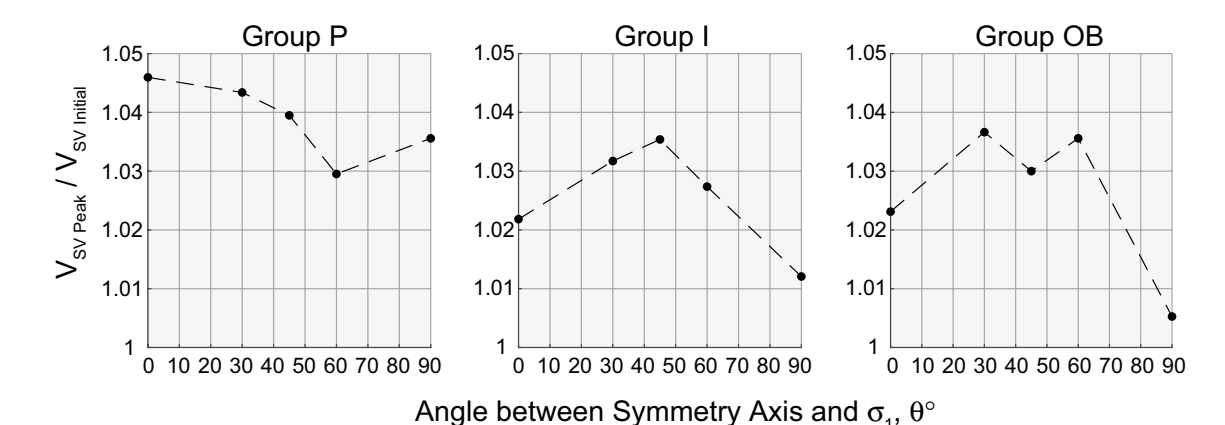


Fig. 9 $V_{\rm SV}$ at peak triaxial stress conditions normalized with the $V_{\rm SV}$ at the beginning of triaxial loading. The intermediate orientations in sample groups I and OB have higher normalized velocities compared

to the parallel and perpendicular orientations. In contrast, the intermediate orientations in sample group P generally have lower normalized velocity than parallel and perpendicular orientations

Table 4 Summary of the stress conditions under which Young's modulus and Poisson's ratio were calculated for each sample

Stress boundary condition	Stress path stage #	Confining pressure, P _c (MPa)	Axial differential stress, $\sigma_{Ax. Diff.}$ (MPa)		
			Initial	Final	
Triaxial loading	1	21	1	6	
	2	21	6	16	
	3	21	16	21	
	4	21	21	16	
	5	21	16	6	
	6	21	6	1	
Uniaxial loading	A	0	1	10	
	В	0	10	20	
	C	0	20	30	
	D	0	30	45	

than the perpendicular $(\theta=0^\circ)$ orientation. The difference between parallel and perpendicular Young's modulus is smaller in planar sample group OB than I and P suggesting that the expected degree of anisotropy appears to be smaller in sample group OB. However, the complete range of Young's modulus anisotropy for sample groups I and OB is not adequately captured by the difference between parallel and perpendicular Young's modulus. Intermediate orientations for I and OB show a significant decrease in Young's modulus compared to the parallel and perpendicular sample orientations. The lower Young's modulus indicates that there is a larger amount of axial strain when loaded in the intermediate orientations compared to the parallel and perpendicular orientations. On the other hand, the intermediate orientations

of the P sample group show a monotonic increase in Young's modulus from perpendicular to parallel orientation.

Folded samples show significant variability in Young's modulus across all samples. The variability does not appear to be more significant in one sample group than the other which suggests that variability in Young's modulus is more likely a result of heterogeneity differences across all folded samples rather than differences between the PDB group and the OB group.

Figure 11 shows the Poisson's ratios measured for each of the stress path sections in Table 4. For the planar sample groups, Poisson's ratios from the parallel and perpendicular orientations correspond to the elastic constants ν_{31} , ν_{13} , and ν_{12} . Across all three planar sample groups, the ν_{13} Poisson's ratio measured from the parallel samples is the highest of the three anisotropic Poisson's Ratio suggesting that the lateral deformation is more significant crossing the foliation planes than within the foliation plane when axial load is applied parallel to the foliation planes. Sample group I has the highest variability between ν_{31} , ν_{13} , and ν_{12} which suggests enhanced anisotropy for the ratio of lateral to axial deformation in group I than groups P and OB. Although group OB had a low amount of anisotropy between the parallel and perpendicular Young's moduli, the Poisson's ratios show a variability that is consistent with or greater than the Poisson's ratios in group P.

Comparing the variability of Poisson's ratio from the folded sample groups is difficult because few values were obtained under the same stress state. Overall, the Poisson's ratios fell between 0.08 and 0.26 for the folded samples. As with the Young's modulus, the variability in the Poisson's ratio does not appear to be dependent on sample group as the variability spans across all five samples.



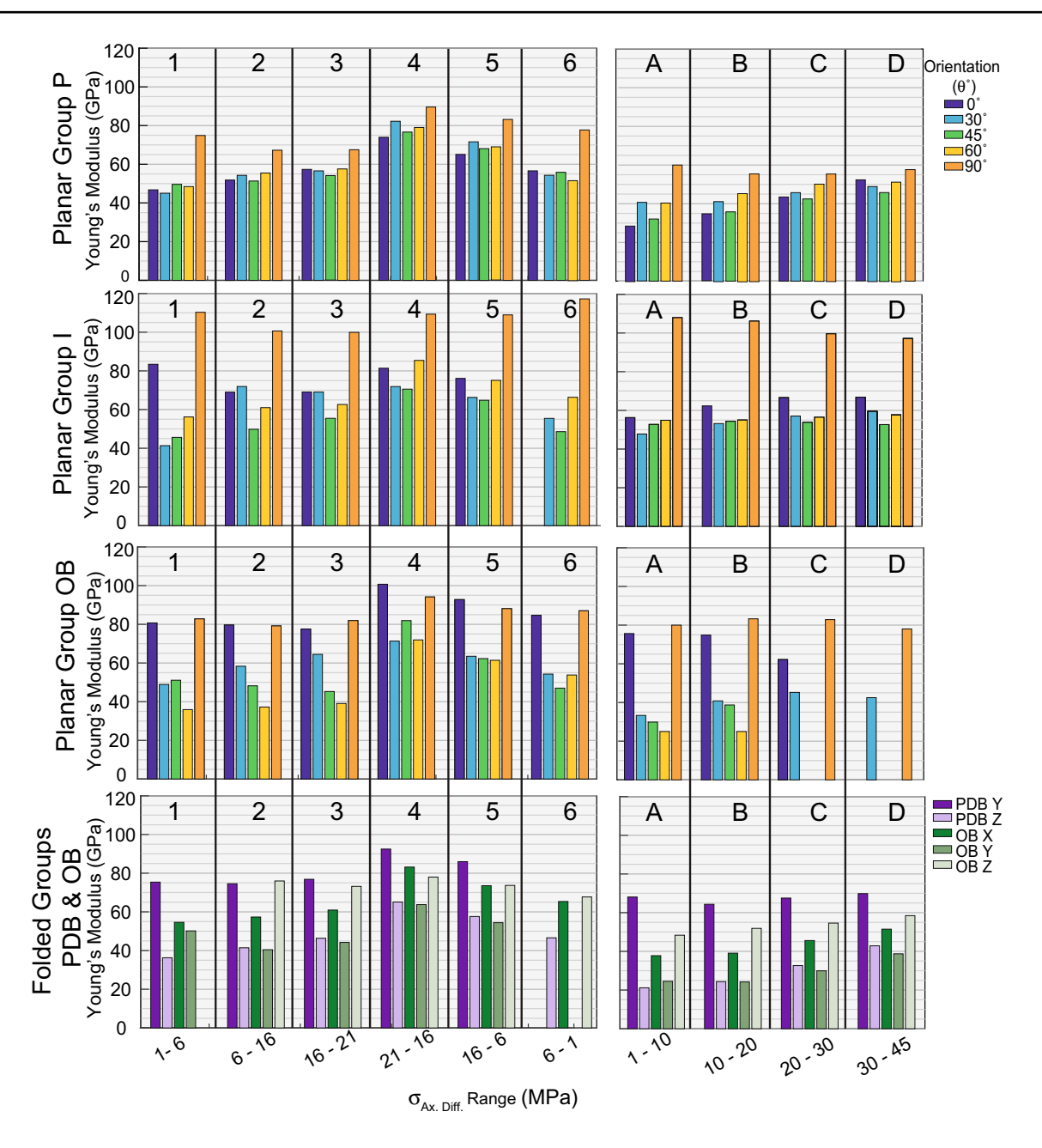


Fig. 10 Young's modulus measured during different stress paths. The first three subplots correspond to planar sample groups whereas the final subplot shows both folded sample groups. The planar samples

are color coded by foliation orientation (θ°) from 0° at the left-most bar and 90° at the right-most bar

4.4 Uniaxial Compressive Strength Results

The uniaxial compressive strength (UCS) of each sample was measured by failing the sample at a constant strain rate after the triaxial stress stages. The test stage protocol in Fig. 6 shows a black "X" which marks the stress at which the sample failed and the UCS was determined. The UCS is plotted against orientation (θ °) for the three planar sample groups in Fig. 12a and against the two folded group categories in Fig. 12b. As previous studies on phyllite have shown,

the uniaxial compressive strength is expected to decrease for intermediate orientations of θ resulting in a "U-shaped" angular dependence of strength. Ramamurthy et al. (1993) utilize an equation adapted from Jaeger (1960) to predict the compressive strength for various orientations using the known compressive strength of three orientations: horizontal (θ =0°), vertical (θ =90°), and the weakest intermediate orientation (typically θ =60°). This equation utilizes a cosine curve fit to the UCS on either side of the weakest sample orientation:



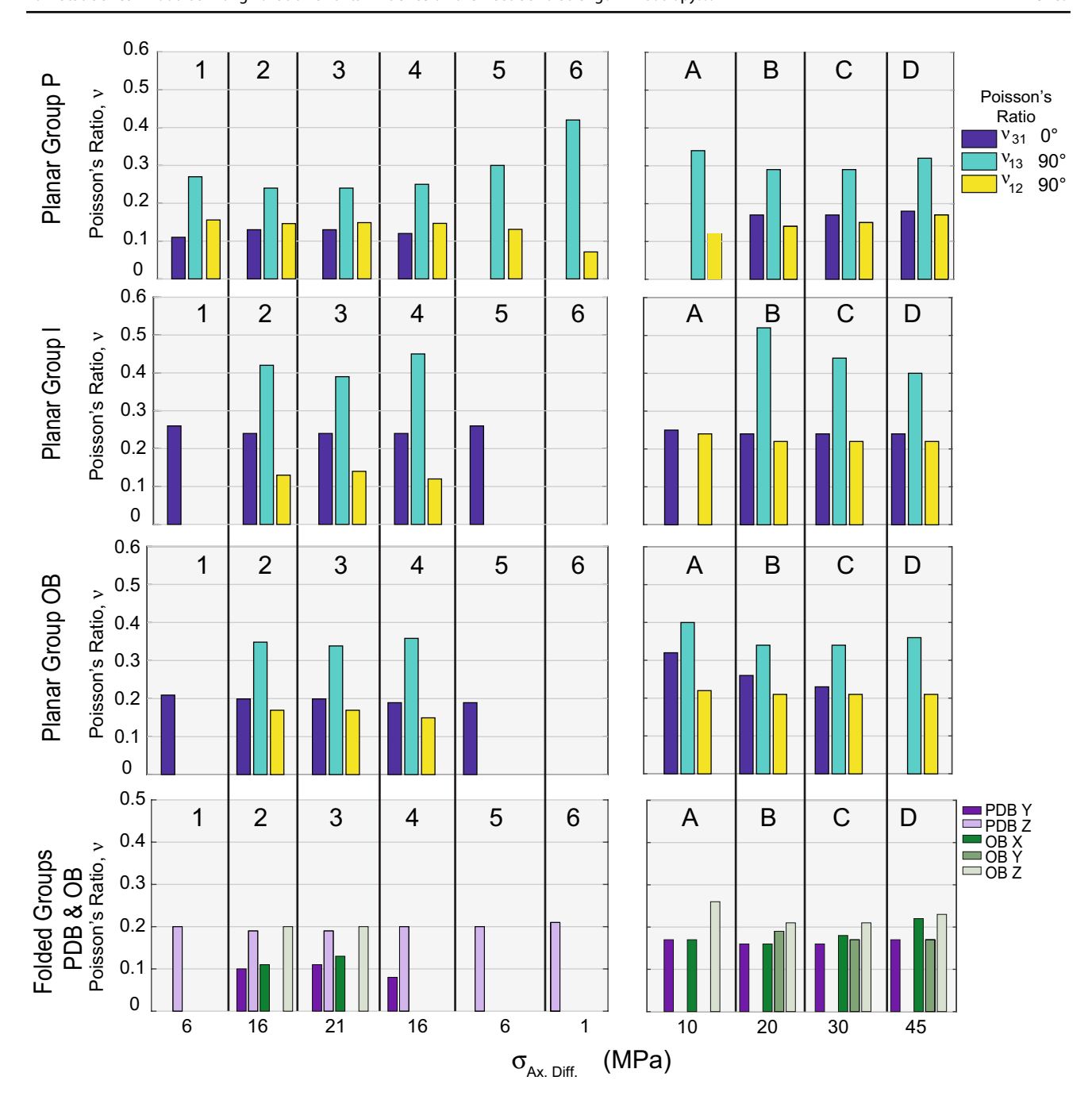


Fig. 11 Poisson's ratio for all sample groups taken at different points of the stress loading path

$$\sigma_{\rm c} = A - B(\cos 2(\theta_{\rm min} - \theta)), \qquad (16)$$

where $\sigma_{\rm c}$ is the uniaxial compressive strength at orientation angle θ , $\theta_{\rm min}$ is the orientation angle for the minimum strength which is either 45° or 60° in our results, A and B are constants describing the variation of the compressive strength either between $\theta = 0^{\circ}$ and $\theta_{\rm min}$ or between $\theta = 90^{\circ}$ and $\theta_{\rm min}$.

Using Eq. (16), the predicted UCS curves were fit to the $\theta = 0^{\circ}$, $\theta = 90^{\circ}$, and θ_{\min} planar sample strengths for each

group. Figure 12a shows that the predicted UCS curves captures the trend of the strength measurements and produce the expected "U" shape for UCS of anisotropic rocks. The maximum strength of sample groups I and OB occurred at θ =90° whereas the maximum strength of sample group P occurred at θ =0°. Table 5 provides the UCS measurements for all samples.

Figure 12b reveals that the UCS for the five folded samples ranges from 93.5 to 144.3 MPa. The 42.7% difference between the maximum and minimum UCS for the PDB



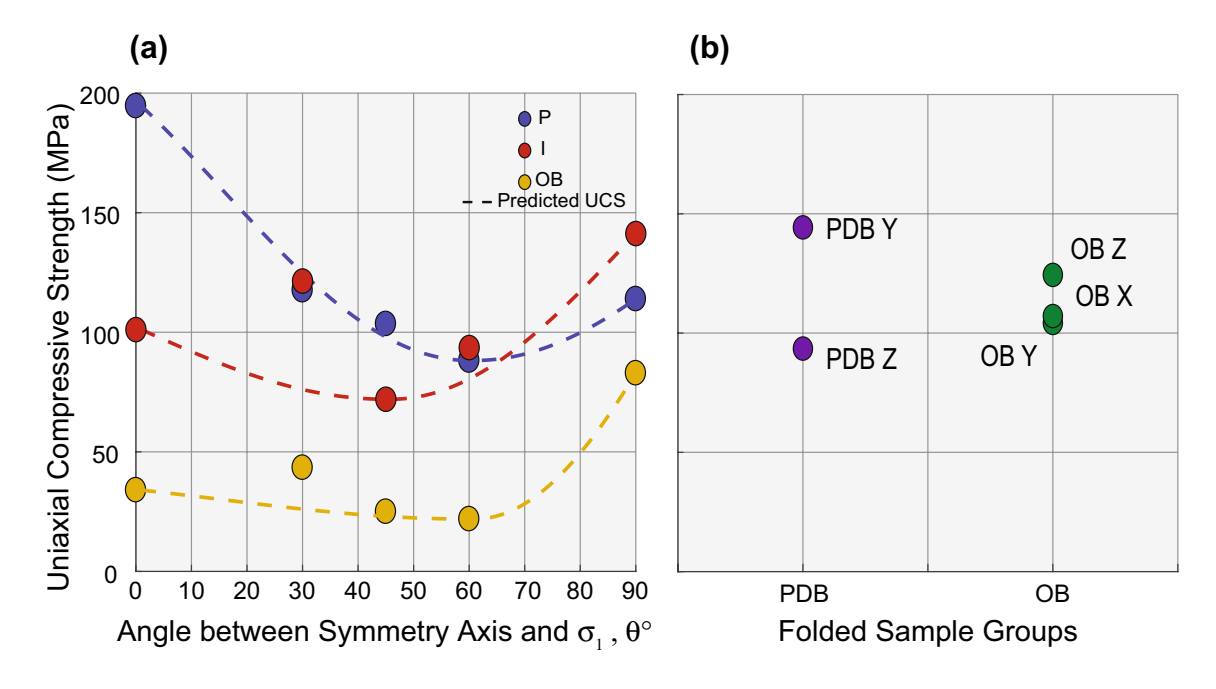


Fig. 12 Uniaxial compressive strength a against foliation orientation θ , for the three planar sample groups and b for the two folded sample groups

 Table 5
 Uniaxial compressive

 strength (UCS) of all samples

Sample name	UCS (MPa)
P0	194.6
P30	117.6
P45	103.5
P60	88.2
P90	113.9
IO	101.1
I30	121.4
I45	72
I60	93.6
I90	141.3
OB0	34
OB30	43.4
OB45	25
OB60	21.9
OB90	82.9
PDB Y	144.3
PDB Z	93.5
OB X	106.1
OB Y	104.2
OB Z	123.4

folded sample groups suggests there is significant variability in the rock strength even in the absence of continuous, planar foliation features. The percent difference between the maximum and minimum UCS is significantly less at 16.9% within the OB folded groups. The variability in UCS appears to be

much higher between the two PDB samples than between the folded OB samples.

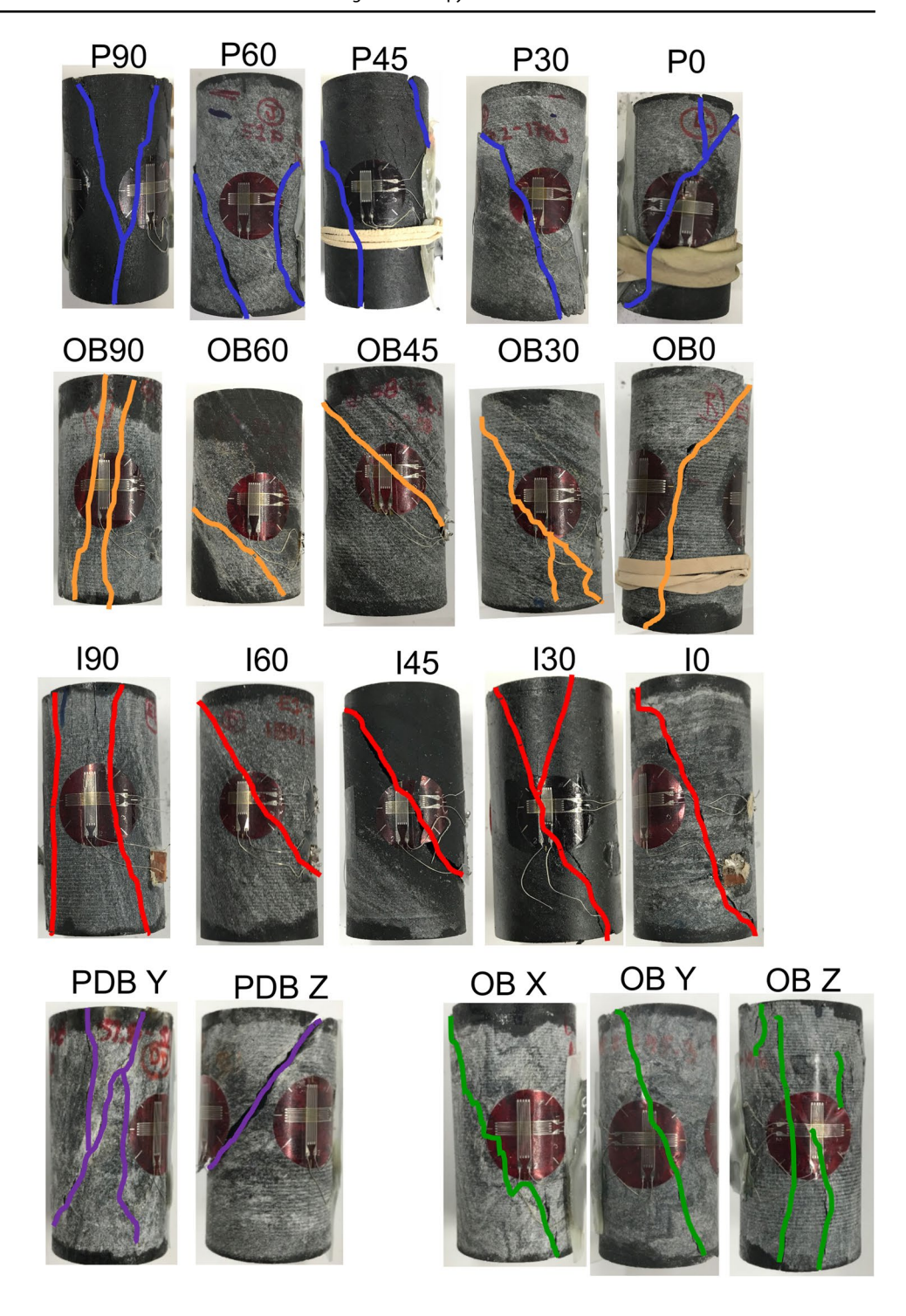
4.5 Influence of Foliation Orientation on UCS and Failure Plane

Examination of the failure planes for the planar sample groups in Fig. 13 suggests that the parallel and perpendicular sample orientation fail through a different failure mode than the intermediate sample orientations. Typically, rock failure in compression is expected to occur via a macroscopic shear failure plane oriented nearly 30° from the sample axis based on the Mohr-Coulomb failure criteria. However, failure under uniaxial stress conditions can typically occur through axial splitting parallel to the orientation of axial stress as well as shear failure. Figure 13 shows samples with foliation oriented parallel to the loading axis failed either by axial splitting or a combination of shear and axial splitting. Perpendicular orientations failed through macroscopic shear failure which cross cut the foliation orientation. Both types of failure planes observed in the parallel and perpendicular samples are consistent with the expected failure mechanisms observed in laboratory measurements.

The 45° and 60° orientations in sample groups I and OB failed through shearing along the foliation plane. This observation is well supported by previous laboratory studies on the strength of anisotropic rocks (Attewell and Sandford 1974; Jaeger 1960; McLamore and Gray 1967; Ramamurthy et al. 1993; Saeidi et al. 2014; Walsh and Brace 1964).



Fig. 13 Images of samples failed under uniaxial stress conditions. Failure planes are highlighted with colored lines to observe the mode of failure



The 45° and 60° orientations serve as weak planes that are more likely to fail prematurely compared to other orientations. The 30° orientation samples in I and OB showed a combination of shear failure along the foliation planes and cross-cutting of the foliations producing slightly irregular macroscopic shear failure planes, marking a transition in failure style from perpendicular samples $(\theta=0^{\circ})$ to intermediate orientation samples $(\theta=45^{\circ},60^{\circ})$.

The failure planes of the 45° and 60° orientations in the P sample group were different from I and OB sample groups, showing some influence of the foliation plane orientation but not a clear shear failure aligned with the foliation. This may be influenced by the relative distinctiveness of the foliation planes in sample group P compared to I and OB. Photographs of the samples in Fig. 4 show that the foliation planes in sample group P are somewhat less planar and continuous



than the foliation planes in I and OB. Photomicrographs of the samples in Fig. 5 also show that the foliation bands are not well defined in sample group P.

The majority of failure planes from the folded samples were either axial splitting or a macroscopic shear failure plane as seen in Fig. 13. It is consistently observed that samples that fail by axial splitting are stronger than those failing by shear along an oblique plane. The difference is especially clear in the two samples in PDB, where PDB Z with a relatively smooth shear failure plane is significantly weaker than PDB Y which failed via a complex network of axial splitting and shear failure planes. Note that the PDB Z sheared along a faint foliation plane that was only observed post-failure. The failure behavior of the folded samples suggest that the eventual geometry of the failure plane has a strong control on the rock strength although not obvious initially due to the random folded texture of the sample.

5 Discussion

5.1 Comparison of Static and Dynamic Young's Modulus

5.1.1 Stress State Considerations

To compare the static and dynamic elastic properties of anisotropic rocks, careful consideration must be brought to select data from the appropriate stage in the experiment. We compare the static Young's modulus measured during stage 1 described in Fig. 10 with the dynamic Young's modulus calculated from velocities before the initiation of stage 1 when the stress state was hydrostatic. These two stress states provide the most similar conditions for comparing static and dynamic elastic properties of an anisotropic rock.

Dynamic measurements targeted at capturing the intrinsic anisotropy of the rock require that samples are under the same principal stress orientations and magnitudes because an anisotropic stress state introduces additional elastic anisotropy due to preferential alignment of open and closed cracks (Nur and Simmons 1969). A restriction in our experimental setup is that the direction of wave propagation is coupled with the direction of applied differential stress. Thus, rotation of the foliation orientation with respect to the sample cylindrical axis not only changes the wave propagation direction, but also results in rotation of the principal stress direction relative to the foliation plane if any axial differential stress is applied. Therefore, dynamic anisotropic elastic properties are only properly derived from measurements under a hydrostatic stress state.

On the other hand, measurement of the static Young's modulus requires the application of an axial differential stress to measure the axial deformation. Thus, stress-induced

anisotropy is an inevitable outcome of static measurements. We minimize stress-induced anisotropy by applying between 1 and 6 MPa of axial differential stress under 21 MPa of confining pressure when measuring static Young's modulus.

5.1.2 Variability in the Behavior of Static Young's Modulus at Intermediate Orientations

We compare the static and dynamic Young's modulus as a function of foliation orientation for the three planar sample groups. Velocity measurements yield the complete dynamic stiffness matrix which was inverted to obtain the complete dynamic compliance matrix. Then Eq. (14) was utilized to predict the dynamic Young's modulus for any foliation orientation using components of the dynamic compliance matrix. The red curve in Fig. 14 shows the predicted dynamic Young's modulus variation with foliation orientation. The behavior of the dynamic Young's modulus curve is the same for all three sample groups and shows an increase in dynamic Young's modulus from perpendicular to parallel orientations.

For sample group P, the dynamic Young's modulus curve follows a relatively similar monotonically increasing trend as the measurements of static Young's modulus marked by the black dots and gray bars. However, there is a significant discrepancy in trend between the predicted dynamic and the measured static Young's modulus for groups I and OB. Compared to parallel and perpendicular orientations, the intermediate orientations show a significant decrease in static Young's modulus for the I and OB sample groups which is not present in the predicted dynamic measurement curve. Some previous laboratory works have also observed a decreased static Young's modulus at intermediate orientations for schistose rocks (Read et al. 1987), but an explanation regarding the source of this behavior is not provided.

We use Eq. (14) to fit elastic moduli parameters using a least-squares approach to the static Young's modulus measurements for the three sample groups. Because the values for static Young's moduli E_1 and E_3 and Poisson's ratio ν_{31} were already known from the parallel and perpendicular orientation measurements, these values were fixed leaving G_{13} as the fitting parameter in the least-square regression. The static moduli resulting from the fit are provided with the dynamic moduli in Table 6 and the Young's modulus results from the parameter fit are shown with the black dashed line in Fig. 14. A comparison of the static and dynamic moduli reveals that the static G_{13} shear modulus is significantly lower than the dynamic G_{13} for sample groups I and OB. Sample group P shows a 31.7% decrease from dynamic to static G_{13} compared to a 56.5% decrease in sample group I and a 57.3% decrease in group OB. These results indicate that it is the significantly lower static G₁₃ values in groups I and OB that control the U-shaped Young's modulus decrease at intermediate orientations. This is sensible because shear stress



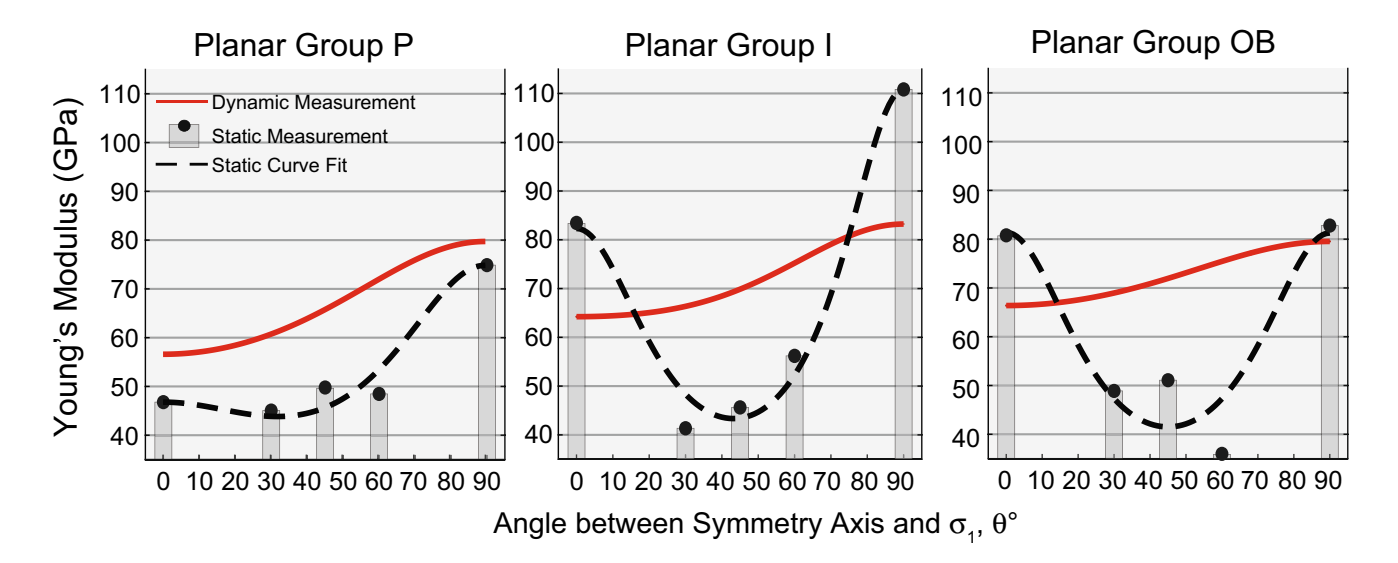


Fig. 14 Static and dynamic Young's modulus fit for all orientations of θ . The dynamic measurement curve was obtained from the complete set of compliance matrix components and the analytical solution presented in Sect. 2.3. Static measurements for Young's mod-

ulus are shown as gray bars with a curve fit using a least-squares method. The black dashed line represents a curve fit with tight bounds on the 0° and 90° sample orientations (E_{33} and E_{11}) and the ν_{31} Poisson's ratio

Table 6 Elastic constants from the complete dynamic compliance components and a curve fit performed on the static Young's modulus for various orientations. The analytical expression provided in Sect. 2.3 is used to obtain the Young's modulus curve in all orienta-

tions. The E_1 , E_3 , and ν_{31} values were fixed while fitting the Young's modulus curve because the values were readily available from the laboratory measurements

Planar group	P		I		ОВ	
Curve fit measurement	Dynamic moduli	Static moduli from curve fit	Dynamic moduli	Static moduli from curve fit	Dynamic moduli	Static moduli from curve fit
$\overline{E_1}$	79.81	74.87	83.23	110.29	79.54	82.79
E_3	56.59	46.78	64.24	83.42	66.38	80.7
v ₃₁	0.26	0.11	0.13	0.26	0.17	0.21
G_{13}	24.99	17.15	29.73	12.92	30.32	12.94

resolved along the foliation planes is greater for intermediate orientations, resulting in enhanced static shear strain along the foliation plane, greater measured axial strain, and lower apparent static Young's modulus.

The E_{Dynamic} versus E_{Static} plot in Fig. 15 more clearly shows the contrast in Young's modulus behavior between the parallel and perpendicular orientations and the intermediate orientations observed in Fig. 14. The one-to-one correspondence of dynamic and static Young's modulus is shown with a black line and 10% differences are shown as dashed lines. The intermediate orientation data plot above the 10% difference line showing that the dynamic Young's modulus is significantly higher than the static Young's modulus. On the other hand, the parallel and perpendicular sample orientations either plot within or below the 10% difference lines showing the static Young's modulus is similar or slightly higher than the dynamic Young's modulus.

5.1.3 Cause of Low Static G_{13} Shear Modulus

The low static G_{13} shear modulus in the I and OB sample groups is a result of enhanced static shear deformation that occurs parallel to the foliation plane. In addition to the regression analysis of static Young's modulus in the previous section, there are several lines of evidence and information that suggest such foliation-parallel shear deformation.

Velocity increase and rock stiffening associated with stress increase is generally attributed to crack closure. Therefore, in a TI rock, perpendicular samples (θ =0°) are typically expected to show the highest degree of stiffening because there are more cracks aligned normal to the applied differential stress that can close with additional axial stress. However, velocity measurements presented in Sect. 4.2 show larger degree of stiffening in the intermediate orientations than the perpendicular orientations for the I and OB



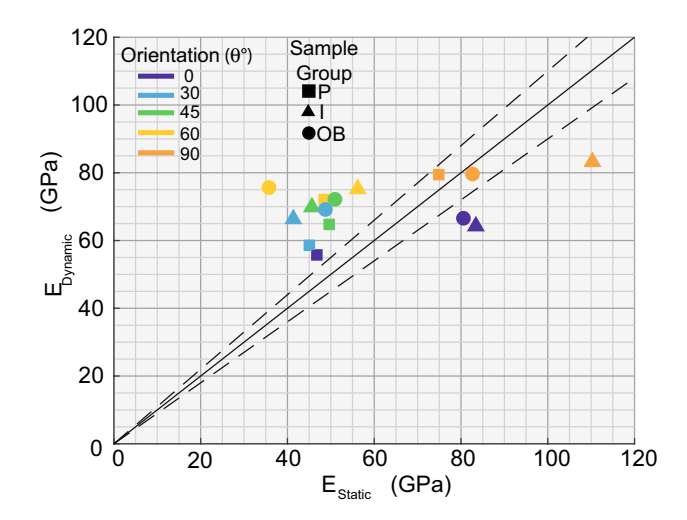


Fig. 15 Comparison of dynamic and static Young's modulus for the three planar sample groups. The solid line represents one to one correspondence and the dashed lines are 10% differences

samples. Thus, stiffening seen in the normalized velocity measurements that exceed the perpendicular sample orientation (θ =0°) is likely caused by some additional deformation rather than crack-normal closure. This is also evident from the observation that there was more hysteresis in velocity data after unloading in many intermediate orientation samples than in the perpendicular samples for I and OB sample groups (Fig. 8).

We suggest that the most likely mechanism by which intermediate orientation samples can become stiffer is through shear slip along the foliation planes. Shear slip is favorable since it involves minimal volume change if the slip plane is smooth and it can potentially lead to shear-enhanced compaction by closing foliation-normal cracks between edges of the platy minerals forming the foliated fabric (Fig. 16). Note that the compaction sketched in Fig. 16a, b can be accomplished only by shear slip along foliation interfaces that have the same sense of shear as the

far-field shear deformation. At intermediate orientations, the shear stress acting along the foliation plane is greater than parallel and perpendicular orientations, so there is greater tendency for shear slip to occur. Shear slip should also occur preferentially along clay minerals that define the foliation fabric because of their low coefficient of friction (Moore and Lockner 2004).

Sample group P does not exhibit similar enhanced stiffening behavior at intermediate angles, which suggests that less shear slip occurred for intermediate orientations in sample group P. Photomicrographs in Fig. 5 show that there are more continuous foliation planes containing weak minerals in groups I and OB compared to group P. The I and OB group samples show that the clay minerals are aligned as straight continuous planes compared to sample group P where there is a significant presence of small clay minerals that are well incorporated into the rock matrix. Foliation in sample group P is more undulating at the sub-millimeter scale. We suspect under large strains, weak clay minerals distributed as short, non-continuous, irregular planes are less effective at facilitating shear slip than when the clay minerals are distributed as smooth continuous foliation planes in the rock. This is also supported by the fact that failure planes of intermediate orientation samples in group P are more irregular than those in groups I and OB (Fig. 13), resulting in higher UCS in sample group P than in groups I and OB (Fig. 12). The same can be observed from the folded samples where those with irregular failure planes resulted in higher UCS. Thus, the presence of continuous, distinct foliation planes of weak clay minerals present in sample groups I and OB, but not in sample group P, explains the anomalously low static shear modulus in sample groups I and OB, and also their peculiar trend of Young's modulus with foliation orientation.

5.1.4 Implications for Hydro-shearing and Stimulation

Frash et al. (2019) suggests that the foliation of the Poorman Schist is the most likely natural feature that undergo

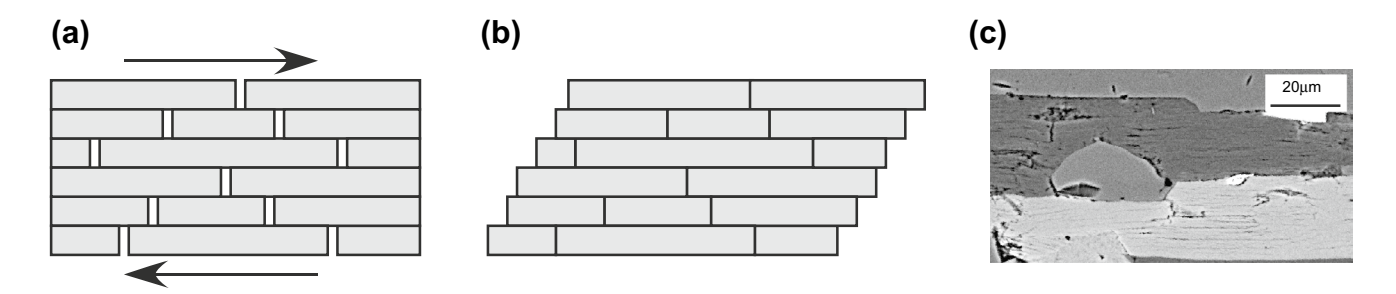


Fig. 16 Schematic describing how shear deformation along smooth foliation planes could lead to shear-enhanced compaction. Note that the transition from the original state in **a** to the compacted state in **b** only required shear slip along the foliation interfaces that has the

same shear sense as the far-field shear deformation shown by the black arrows. c SEM image of some foliation-normal cracks in a Poorman schist sample



hydro-shearing in response to fluid injection and stimulation in the EGS Collab Experiment 1 test bed. Frash et al. (2019) found from their triaxial direct-shear tests that shear strength along foliations (whether unbonded, infilled, or intact) were significantly weaker than infilled natural fractures found in the Poorman Schist at various orientations. Thus, shear strengths of the foliations are reached before injected fluid pressure reaches the minimum principal stress to create mode-I hydraulic fractures.

Our results are consistent with this notion and further suggests that enhanced shear slip along foliations may occur from the very beginning of the injection process well before the shear stress reaches the short-term shear strength of the rock and hydro-shearing is achieved. Already in the first loading stage of our experiment (stress path stage 1), low static shear modulus along foliation planes was evident in all sample groups from the low static G₁₃ shear moduli values compared to their dynamic counterparts, even in sample group P (Table 6). This implies premature shear slip along foliations that may explain why foliation planes are weak in these rocks and later promotes hydro-shearing over mode-I hydraulic fracturing.

Furthermore, if this premature shear slip occurs at a large enough magnitude, this may also imply appreciable permeability change and stimulation well before macroscopic hydro-shearing is achieved by injection, an important implication for engineering reservoir stimulation by fluid injections. However, it is not trivial to address this problem as we imply shear-enhanced compaction as a mechanism to explain the simultaneous occurrence of enhanced shear deformation (low static G_{13}) and overall stiffening of the rock (greater hysteresis in intermediate orientations of groups I and OB). Under shear-enhanced compaction, there is likely a competition between local shear dilatancy and overall compaction that governs the permeability change of the rock. Also, any permeability change caused by the premature shear slip along the foliation is likely highly anisotropic. Thus, the resulting stimulation effect is also anisotropic. Careful investigation through further deformation experiments with simultaneous permeability measurements is needed for quantitative evaluation.

5.2 Laboratory Measurements of Heterogeneous Rock and Complications from Similar Scale

The purpose of measuring the elastic properties from the folded samples was to determine if the rock behaves as an apparently homogeneous isotropic material due to the lack of a distinct orientation of foliation and folding. From the variability of the static and dynamic Young's moduli and Poisson's ratio, it is apparent that heterogeneity plays a significant role in determining elastic properties. Heterogeneities in the folded laboratory samples are present at 1 cm

scale. Strain gages with 1 cm length measure a local strain response at the same length scale of the folded features rendering static elastic properties that are influenced by sample heterogeneities. Velocity measurements are influenced by the similar length scale of the heterogeneous features with the ultrasonic wavelength. For example, an ultrasonic frequency of 200 kHz has a 2.5-cm wavelength for a material with 5000 m/s velocity. When the wavelength is comparable to the length scale of heterogeneities, the measured velocity is more sensitive to variability in material properties compared to a wavelength that is significantly larger than the heterogeneities. Variability in the velocity measurements of the folded samples can be observed in Fig. 7 where there is nearly a 1000 m/s difference between the minimum and maximum V_P. Due to the sensitivity of laboratory measurements to the folded sample heterogeneities, representative isotropic elastic properties were not obtained.

In the field, sonic logging tools measure velocities along the length of the borehole. Sonic velocities in the field are measured with a lower frequency compared to the ultrasonic velocities measured in the laboratory. Understanding the influence of measurement frequency and scale of heterogeneities on velocity is necessary to accurately interpret any potential differences in velocity at the laboratory and field scale. Laboratory measurements at both the same scale and larger scale to the heterogeneous features could help understand how sensitive field measurements would be to heterogeneous features present at a range of scales. The issue of scale is a consistent challenge in rock mechanics applications where mechanical properties are often measured at laboratory scale and applied to the field scale.

6 Conclusion

In this study, we provided laboratory measurements for dynamic elastic properties, static Young's modulus, Poisson's ratio, and unconfined compressive strength on Poorman schist rocks with planar and folded foliations. The planar sample groups were expected to have symmetry consistent with transversely isotropic medium where five independent elastic constants are needed to fully describe the mechanical behavior. A complete solution for the Young's modulus of a transversely isotropic medium at any orientation with respect to the loading direction is provided in the Appendix A and utilized in this paper to evaluate the influence of orientation on the elastic properties. From our measurements, we conclude that

For schist rocks with continuous, planar foliations, 45° and 60° foliation planes act as weak planes that facilitate shear failure along the foliation orientation instead of cross-cutting the foliation planes.



The G_{13} shear modulus of a TI medium can be determined from Young's modulus measurements with foliation parallel, perpendicular, and oblique to the loading direction.

Low static Young's modulus for schist rocks at intermediate foliation orientations can result from anomalously low apparent static shear modulus, caused by shear slip along distinct sharp foliation planes.

Laboratory measurements on folded rocks demonstrated the sensitivity of measurements to heterogeneous features in the rock when the features were at a similar scale to the measuring devices.

Acknowledgements This material was based upon work supported by the U.S. Department of Energy, Office of Energy Efficiency and Renewable Energy (EERE), Office of Technology Development, and Geothermal Technologies Office under Award Number DE-AC02-05CH11231 with LBNL. The United States Government retains, and the publisher, by accepting the article for publication, acknowledges that the United States Government retains a non-exclusive, paid-up, irrevocable, world-wide license to publish or reproduce the published form of this manuscript, or allow others to do so, for United States Government purposes. The research supporting this work took place in whole or in part at the Sanford Underground Research Facility in Lead, South Dakota. The assistance of the Sanford Underground Research Facility and its personnel in providing physical access and general logistical and technical support is acknowledged. We thank Megan Smith for providing XRD mineralogy results of the samples used in this study.

Compliance with Ethical Standards

Conflict of interest The authors declare that they have no conflict of interest.

Appendix A: Analytical Expression for Young's Modulus of Rotated TI Mediums

1. Uniaxial stress is applied in the x_3 -direction making σ_{33} the only nonzero stress in the initial x_1 – x_3 coordinate system.

2. Rotate the stress matrix about the
$$x_2$$
-axis to the x_1' - x_3' coordinate system. The rotation matrix, R , is given from the direction cosines between the initial and prime axis.

$$R = \begin{bmatrix} \cos\theta & \cos90 & \cos(\theta + 90) \\ \cos90 & \cos0 & \cos90 \\ \cos(90 - \theta) & \cos90 & \cos\theta \end{bmatrix} = \begin{bmatrix} \cos\theta & 0 & -\sin\theta \\ 0 & 1 & 0 \\ \sin\theta & 0 & \cos\theta \end{bmatrix},$$

$$\begin{split} \sigma' &= R\sigma R^{-1} = \begin{bmatrix} \cos\theta & 0 & -\sin\theta \\ 0 & 1 & 0 \\ \sin\theta & 0 & \cos\theta \end{bmatrix} \begin{bmatrix} 0 & 0 & 0 \\ 0 & 0 & 0 \\ 0 & 0 & \sigma_{33} \end{bmatrix} \begin{bmatrix} \cos\theta & 0 & \sin\theta \\ 0 & 1 & 0 \\ -\sin\theta & 0 & \cos\theta \end{bmatrix} \\ &= \begin{bmatrix} \sin^2\theta & 0 & -\sin\theta\cos\theta \\ 0 & 0 & 0 \\ -\sin\theta\cos\theta & 0 & \cos^2\theta \end{bmatrix} \sigma_{33}. \end{split}$$

3. Rewrite the rotated stress matrix in Voigt notation and multiply the compliance matrix by the rotated stress matrix to find the strain in the prime coordinate system.

$$\varepsilon' = S * \sigma',$$

$$\begin{bmatrix} \varepsilon_{11}' \\ \varepsilon_{22}' \\ \varepsilon_{33}' \\ 2\varepsilon_{23}' \\ 2\varepsilon_{12} \end{bmatrix} = \begin{bmatrix} s_{11} & s_{12} & s_{13} & 0 & 0 & 0 \\ s_{12} & s_{11} & s_{13} & 0 & 0 & 0 \\ s_{13} & s_{13} & s_{33} & 0 & 0 & 0 \\ 0 & 0 & 0 & s_{44} & 0 & 0 \\ 0 & 0 & 0 & 0 & s_{44} & 0 \\ 0 & 0 & 0 & 0 & 0 & s_{66} \end{bmatrix} * \begin{bmatrix} \sin^2\theta \\ 0 \\ \cos^2\theta \\ 0 \\ -\sin\theta\cos\theta \\ 0 \end{bmatrix} \sigma_{33},$$

$$\epsilon' = \begin{bmatrix} s_{11}\sin^2\theta + s_{13}\cos^2\theta & 0 & -\frac{s_{44}\sin\theta\cos\theta}{2} \\ 0 & s_{12}\sin^2\theta + s_{13}\cos^2\theta & 0 \\ -\frac{s_{44}\sin\theta\cos\theta}{2} & 0 & s_{13}\sin^2\theta + s_{33}\cos^2\theta \end{bmatrix} \sigma_{33}$$

4. Rotate the strain tensor back to the initial coordinate system using the inverse rotation matrix R^{-1} .

$$\varepsilon = R^{-1} \varepsilon' R$$
.

$$\varepsilon = \begin{bmatrix} \cos\theta & 0 & \sin\theta \\ 0 & 1 & 0 \\ -\sin\theta & 0 & \cos\theta \end{bmatrix} \begin{bmatrix} s_{11} \sin^2\theta + s_{13} \cos^2\theta & 0 & -\frac{s_{44} \sin\theta\cos\theta}{2} \\ 0 & s_{12} \sin^2\theta + s_{13} \cos^2\theta & 0 \\ -\frac{s_{44} \sin\theta\cos\theta}{2} & 0 & s_{13} \sin^2\theta + s_{33} \cos^2\theta \end{bmatrix} \sigma_{33} \begin{bmatrix} \cos\theta & 0 & -\sin\theta \\ 0 & 1 & 0 \\ \sin\theta & 0 & \cos\theta \end{bmatrix}.$$

$$\begin{bmatrix} -\frac{s_{44}\sin\theta\cos\theta}{2} \\ 0 \\ s_{13}\sin^{2}\theta + s_{33}\cos^{2}\theta \end{bmatrix} \sigma_{33} \begin{bmatrix} \cos\theta & 0 & -\sin\theta \\ 0 & 1 & 0 \\ \sin\theta & 0 & \cos\theta \end{bmatrix}.$$

$$\sigma = \begin{bmatrix} \sigma_{11} & \sigma_{12} & \sigma_{13} \\ \sigma_{12} & \sigma_{22} & \sigma_{23} \\ \sigma_{13} & \sigma_{23} & \sigma_{33} \end{bmatrix} = \begin{bmatrix} 0 & 0 & 0 \\ 0 & 0 & 0 \\ 0 & 0 & \sigma_{33} \end{bmatrix}.$$

The individual components of the resulting strain matrix are written in the equations below:

$$\varepsilon_{11} = \left(s_{11}\sin^2\theta\cos^2\theta + s_{13}\left(\sin^4\theta + \cos^4\theta\right) + s_{33}\sin^2\theta\cos^2\theta - s_{44}\sin^2\theta\cos^2\theta\right)\sigma_{33},$$



$$\begin{split} \varepsilon_{22} &= \left(s_{12} \sin^2 \theta + s_{13} \cos^2 \theta \right) \sigma_{33}, & s_{11} &= \frac{1}{E_1}, \\ \varepsilon_{33} &= \left(s_{11} \sin^4 \theta + 2 s_{13} \sin^2 \theta \cos^2 \theta + s_{33} \cos^4 \theta + s_{44} \sin^2 \theta \cos^2 \theta \right) \sigma_{33}, \\ s_{13} &= \frac{-v_{31}}{E_3} = \frac{-v_{13}}{E_1}, \end{split}$$

$$\varepsilon_{13} = \left(-s_{11} \sin^3 \theta \cos \theta + s_{13} \left(\sin^3 \theta \cos \theta - \sin \theta \cos^3 \theta \right) + s_{33} \sin \theta \cos^3 \theta + s_{44} \frac{(\sin^3 \theta \cos \theta - \sin \theta \cos^3 \theta)}{2} \right) \sigma_{33},$$

$$\varepsilon_{12} = 0$$
.

 $\varepsilon_{23}=0$,

5. The Young's modulus is determined from dividing the applied stress by strain in the same direction

$$E = \sigma_{33}/\varepsilon_{33}$$

and can be written in the following convenient form by substituting the compliance matrix components.

$$\varepsilon_{33} = \left(\frac{\sin^4\theta}{E_1} - \frac{2\nu_{31}\sin^2\theta\cos^2\theta}{E_3} + \frac{\cos^4\theta}{E_3} + \frac{\sin^2\theta\cos^2\theta}{G_{13}}\right)\sigma_{33},$$

where for a transverse isotropic material with symmetric axis in the three directions

$$s_{33} = \frac{1}{E_3},$$

$$s_{44} = \frac{1}{G_{13}} = \frac{1}{G_{23}}.$$

Appendix B: Sample Locations and Borehole Diagram

Figure 17 shows the borehole diagram along the west drift on the 4850-ft depth level of SURF adapted from Morris et al. (2018) with discs that indicate the intended notch

Fig. 17 A 3D schematic of the boreholes at the project site along the west access drift on the 4850 ft depth level of SURF. Square markers show the location of the planar sample groups and circle markers show the location of the folded sample groups within the testbed (borehole diagram adapted from Morris et al. 2018)

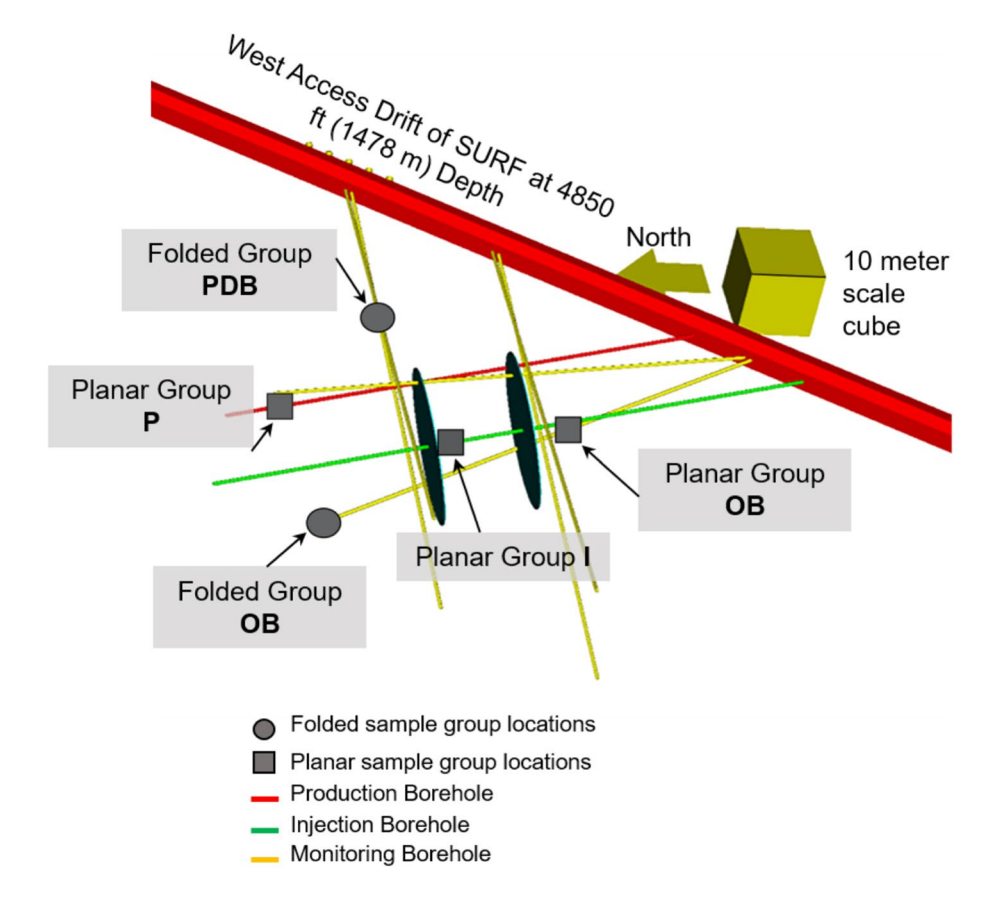




Table 7 Sample depths measured along the borehole axis taken from core logs, photographs, and markings on the host core

Borehole	Sample name	Top depth (ft)	Bottom depth (ft)	Top depth (m)	Bottom depth (m)
E1-P	P90	175.7	175.85	53.6	53.6
E1-P	P60	176.5	176.6	53.8	53.8
E1-P	P45	176.3	176.4	53.7	53.8
E1-P	P30	176.2	176.3	53.7	53.7
E1-P	P0	176.7	176.9	53.9	53.9
E1-I	190	150.9	151.1	46.0	46.1
E1-I	I60	150.1	150.3	45.8	45.8
E1-I	I45	153	153.15	46.6	46.7
E1-I	I30	152.7	152.8	46.5	46.6
E1-I	10	154.6	-	47.1	-
E1-OB	OB90	85.4	85.6	26.0	26.1
E1-OB	OB60	86.5	86.7	26.4	26.4
E1-OB	OB30	87.9	88.1	26.8	26.9
E1-OB	OB0	89.5	_	27.3	_
E1-PDB	PDB Y	51.8	_	15.8	_
E1-PDB	PDB Z	51.1	51.3	15.6	15.6
E1-OB	OB X	195.4	_	59.6	_
E1-OB	ОВ Ү	195.2	195.3	59.5	59.5
E1-OB	OB Z	196	196.2	59.7	59.8

locations for hydraulic stimulation in the EGS Collab project. The testbed is comprised of eight sub-horizontal boreholes oriented around the intended stimulation zone. Sample locations are marked with a square for the planar sample groups and a circle for the folded sample groups. Sample names are assigned based on the borehole and sample orientation. The first letters (P, I, OB, or PDB) indicate the borehole and the second numbers or letters (ex: 0, 45, *X*, *Z*)

indicate the sample orientation. The sample depths along the length of the borehole are provided in Table 7.

Appendix C: Ultrasonic Velocity and Static Young's Modulus Table

See Tables 8 and 9.



Table 8 Sample length, diameter, density and velocity measurements under hydrostatic, triaxial, and uniaxial stress conditions

		`	•		•	,	,					
Sample	Length	Diameter	Density (g/	Velocity unc	ty under hydrostatic stress	stress		Velocity under triaxial stress	ssa	Velocity unc	Velocity under uniaxial stress	ses
name	(mm)	(mm)	cc)	$\sigma_{\text{Ax. Diff.}} = 0$	$=0$ MPa, $P_{\rm C}$ = 21 MPa	MPa	I	$\sigma_{\text{Ax. Diff.}} = 21 \text{ MPa}, P_{\text{C}} = 21 \text{ MPa}$	1 MPa	$\sigma_{\mathrm{Ax.\ Diff.}} = 10$	$\sigma_{Ax. Diff.} = 10-15 \text{ MPa}, P_C = 0 \text{ MPa}$	=0 MPa
				$V_{\rm P}$ (km/s)	$V_{\text{SV}} = V_{\text{S1}}$ (km/s)	$V_{\rm SH} = V_{\rm S2}$ (km/s)	_V _P (km/s)	$V_{\text{SV}} = V_{\text{S1}}$ (km/s)	$V_{\rm SH} = V_{\rm S2}$ (km/s)	$V_{\rm p}$ (km/s)	$V_{\text{SV}} = V_{\text{S1}}$ (km/s)	$V_{\text{SH}} = V_{\text{S2}}$ (km/s)
P0	46.1	25.54	2.768	5.07	3.09	2.95	5.52	3.08	3.15	4.75	2.96	3.04
P30	50.71	25.53	2.760	5.70	3.01	3.29	5.70	3.14	2.96	5.02	2.74	3.14
P45	50.73	25.54	2.762	5.58	2.99	2.99	5.88	3.12	3.15	5.09	2.85	3.04
P60	50.72	25.54	2.755	5.60	3.20	3.43	5.92	3.13	3.15	5.25	3.00	3.04
P90	50.71	25.53	2.748	6.12	2.89	3.51	6.10	3.15	3.40	5.62	3.16	3.17
10	51.89	25.54	2.756	5.06	3.34	3.25	5.18	3.43	3.33	4.94	3.32	3.20
I30	48.42	25.54	2.759	5.02	3.23	3.31	5.24	3.35	3.38	4.94	3.24	3.27
145	50.76	25.54	2.784	5.11	3.28	3.35	5.20	3.38	3.46	4.95	3.24	3.30
09I	52.45	25.52	2.756	5.30	3.44	3.52	5.41	3.53	3.61	5.21	3.41	3.52
061	51.31	25.52	2.764	5.82	3.48	3.69	5.82	3.52	3.72	5.72	3.47	3.70
OB0	50.53	25.53	2.759	5.18	3.32	3.33	5.38	3.40	3.42	5.08	3.32	3.34
OB30	42.83	25.53	2.745	4.69	2.87	2.87	4.88	2.99	2.99	4.47	2.79	2.84
OB45	48.12	25.52	2.750	5.13	3.22	3.39	5.30	3.30	3.44	4.94	3.12	3.25
OB60	43.95	25.54	2.847	4.79	2.84	3.03	5.02	2.93	3.11	4.41	2.48	2.92
OB90	50.96	25.52	2.789	5.61	3.41	3.63	5.66	3.46	3.68	5.62	3.41	3.60
PDB Y	50.41	25.55	2.768	5.88	2.84	3.32	20.9	2.93	3.61	5.49	2.77	3.34
PDB Z	44.86	25.49	2.772	4.57	2.78	2.75	5.40	2.95	2.97	4.51	2.58	1.36
OB X	49.49	25.55	2.746	5.62	3.00	2.88	5.95	3.12	2.98	5.07	2.69	2.76
OB Y	50.39	25.54	2.739	ı	ı	ı	ı	I	ı	ı	ı	1
OBZ	51.8	25.54	2.759	5.53	3.09	3.14	5.86	3.23	3.31	I	I	I



Table 9 Static Young's modulus measurements organized by stress phase and sample

Stress phase	Triaxia	l loading		Triaxial	unloadir	ng	Uniaxia	al loading		
P _C (MPa)	21	21	21	21	21	21	0	0	0	0
$\sigma_{Ax.\;Diff} \\ (initial-final, \\ MPa)$	1–6	6–16	16–21	21–16	16–6	6–1	1–10	10–20	20–30	30–45
Sample name										
P0	46.8	51.9	57.4	74.0	65.1	56.6	28.7	34.6	43.5	52.2
P30	45.0	54.3	56.6	82.2	71.6	54.3	40.6	41.4	45.7	49.1
P45	49.6	51.3	54.0	76.7	68.1	55.8	32.1	35.8	42.5	46.0
P60	48.5	55.5	57.6	79.0	68.8	51.7	40.3	45.6	50.2	51.5
P90	74.9	67.3	67.5	89.6	83.2	77.7	60.0	55.7	55.6	57.6
10	83.4	69.0	69.1	81.4	76.1	_	56.3	62.3	66.6	66.8
I30	41.4	71.9	69.1	71.9	66.3	55.4	47.8	53.2	57.1	59.6
I45	45.6	49.8	55.3	76.3	61.3	48.8	52.7	54.4	53.9	52.7
I60	56.2	61.0	62.6	85.4	75.1	66.4	54.9	55.1	56.5	57.7
I90	110.3	100.6	99.9	109.3	109.0	117.2	108.0	106.2	99.6	97.2
OB0	80.7	79.6	77.5	100.7	92.8	84.6	75.7	74.9	62.2	_
OB30	48.9	58.3	64.4	71.3	63.5	54.3	33.3	40.8	45.2	42.5
OB45	51.1	48.2	45.2	81.9	62.3	47.0	29.9	38.7	_	_
OB60	35.9	37.2	39.1	71.9	61.4	53.8	26.1	26.3	_	_
OB90	82.8	79.2	81.9	94.1	88.1	87.0	80.0	83.3	82.8	78.0
PDB Y	75.4	74.6	76.8	92.5	86.0	_	68.1	64.3	67.5	69.8
PDB Z	36.3	41.4	46.4	65.1	57.6	46.6	21.2	24.3	32.7	42.9
OB X	54.6	57.3	60.9	83.2	73.5	65.4	37.8	39.1	45.6	51.5
ОВ Ү	50.2	40.4	44.2	63.8	54.4	_	24.5	24.2	29.9	38.7
OB Z	-	76.0	73.2	78.0	73.7	67.7	48.4	51.9	54.6	58.5

References

Amadei B (1996) Importance of anisotropy when estimating and measuring in situ stresses in rock. Int J Rock Mech Min Sci Geomech Abstr. https://doi.org/10.1016/0148-9062(95)00062-3

Attewell PB, Sandford MR (1974) Intrinsic shear strength of a brittle, anisotropic rock—I: Experimental and mechanical interpretation. Int J Rock Mech Min Sci Geomech Abstr. https://doi.org/10.1016/0148-9062(74)90453-7

Frash LP, Welch NJ, Carey JW; The EGS Collab Team (2019) Geomechanical evaluation of natural shear fractures in the EGS Collab Experiment 1 test bed. In: 53rd US rock mechanics/geomechanics symposium, New York, June 23–26, 2019, ARMA, pp 1819–1829

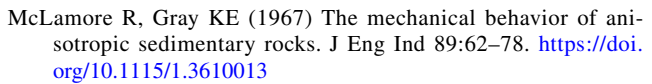
Homand F, Morel E, Henry JP, Cuxac P, Hammade E (1993) Characterization of the moduli of elasticity of an anisotropic rock using dynamic and static methods. Int J Rock Mech Min Sci Geomech Abstr 20:527–535. https://doi.org/10.1016/0148-9062(93)92218-F

Jaeger JC (1960) Shear failure of anisotropic rocks. Geol Mag 97:65–72. https://doi.org/10.1017/S0016756800061100

Jones LEA, Wang HF (1981) Ultrasonic velocities in Cretaceous shales from the Williston basin. Geophysics 46:288–297

Kneafsey TJ, Blankenship D, Knox HA et al (2019) EGS Collab Project: status and progress. In: 44th workshop on geothermal reservoir engineering, Stanford University, Stanford, February 11–13, pp 1–16

Mavko G, Mukerji T, Dvorkin J (2009) The rock physics handbook: tools for seismic analysis of porous media. Cambridge University Press, Second



Moore DE, Lockner DA (2004) Crystallographic controls on the frictional behavior of dry and water-saturated sheet structure minerals. J Geophys Res. https://doi.org/10.1029/2003jb002582

Morris JP, Fu P, Dobson P et al (2018) Experimental design for hydrofracturing and fluid flow at the DOE EGS collab testbed. In: 43rd workshop on geothermal reservoir engineering, Stanford University, Stanford, February 12–14, pp 1–11

Nasseri MHB, Rao KS, Ramamurthy T (2003) Anisotropic strength and deformational behavior of Himalayan schists. Int J Rock Mech Min 40:3–23. https://doi.org/10.1016/S1365-1609(02)00103-X

Nur A, Simmons G (1969) Stress-induced velocity anisotropy in rock: an experimental study. J Geophys Res 74:6667–6674. https://doi.org/10.1029/jb074i027p06667

Nye JF (1985) Physical properties of crystals. Oxford University Press, Oxford

Oldenburg CM, Dobson PF, Wu Y, et al (2017) Hydraulic fracturing experiments at 1500 m depth in a deep mine: highlights from the kISMET project. In: 42nd workshop on geothermal reservoir engineering. pp 1–9

Ramamurthy T, Rao GV, Singh J (1993) Engineering behaviour of phyllites. Eng Geol 33:209–225. https://doi.org/10.1016/0013-7952(93)90059-L

Read SAL, Perrin ND, Brown IR (1987) Measurement and analysis of laboratory strength and deformability characteristics of schistose rocks. In: Proceedings of the sixth international conference on rock mechanics, Montreal, vol 1, pp 233–238



- Saeidi O, Rasouli V, Geranmayeh Vaneghi R et al (2014) A modified failure criterion for transversely isotropic rocks. Geosci Front 5:215–225. https://doi.org/10.1016/j.gsf.2013.05.005
- Sayers CM (2010) The effect of anisotropy on the Young's moduli and Poisson's ratios of shales. In: SEG Denver 2010 annual meeting, pp 2606–2611
- Sone H, Zoback MD (2013) Mechanical properties of shale-gas reservoir rocks—Part 1: Static and dynamic elastic properties and anisotropy. Geophysics 78:D381–D392. https://doi.org/10.1190/GEO2013-0050.1
- Thomsen L (1986) Weak elastic anisotropy. Geophysics 51:1954–1966. https://doi.org/10.1190/1.1442051
- Vigilante P (2017) Rock mechanics laboratory tests relevant to the insitu stress measurements at the 4850-level, Homestake Mine, Lead, South Dakota. M.S. thesis, University of Wisconsin-Madison
- Walsh JB, Brace WF (1964) A fracture criterion for brittle anisotropic rock. J Geophys Res. https://doi.org/10.1029/JZ069i016p03449
- Wang HF, Lee MY, Doe TW, Haimson BC, Oldenburg CM, Dobson PF (2017) In situ stress measurement at 1550-meters depth at the kISMET test site. In: Lead SD (eds) 51st U.S. rock mechanics/geomechanics symposium, San Francisco, CA, 25–28 June 2017, ARMA 17–651

Publisher's Note Springer Nature remains neutral with regard to jurisdictional claims in published maps and institutional affiliations.

